Intrinsic Alkaline OER Activity in Mechanochemically Activated WO_3 from Commercial and Single-Crystal Precursors

Vineetha Vinayakumar[1,2*], Mohit Chatwani[1], Aneeta Jose[1], Osamah Kharsah[2,3], Hao Yun[1], Adithya Aravind[1], Adarsh Jain[1], Ahammed Suhail Odungat[1], Alexander Kunzmann[4,5], Gabi Schierning[2,4,5], Sabrina Disch[2,6], Marika Schleberger[2,3], Doris Segets[1,2*]

1. Institute for Energy and Materials Processes – Particle Science and Technology (EMPI-PST), University of Duisburg-Essen
2. Center for Nanointegration Duisburg-Essen (CENIDE), University of Duisburg-Essen
3. Faculty of Physics, University of Duisburg-Essen, Lotharstraße 1, D-47057 Duisburg, Germany
4. Institute for Energy and Materials Processes – Applied Quantum Materials, University Duisburg-Essen, Duisburg, Germany
5. Research Center Future Energy Materials and Systems (RC FEMS), Research Alliance Ruhr, Bochum, Germany
6. Faculty of Chemistry, University of Duisburg-Essen, Universitätsstraße 15-7, D-45141 Essen, Germany

* V. Vinayakumar, vineetha.vinayakumar@uni-due.de, D.Segets, doris.segets@uni-due.de

Abstract

This study uncovers the interplay between phase-induced interfaces and mechanochemical activation on the alkaline oxygen evolution reaction (OER) performance of tungsten oxide (WO_3). Commercial polycrystalline (WO_3-C) and synthesized single-crystal (WO_3-S) monoclinic WO_3 precursors were subjected to identical mechanochemical processing by planetary ball milling (PBM). Ball-milled single-crystal WO_3 (WO_3-S-PBM) yielded nanocrystalline powders (~20-50 nm) with enriched γ-monoclinic phase content (40% vs. 28% for WO_3-C-PBM), suppressed surface W^{5+} defects, and enhanced hydroxylation. Using Hansen solubility parameters, powders were formulated into stable inks to fabricate OER anodes on Ni substrates. Multi-technique characterization revealed that anodes made from WO_3-S-PBM resulted in continuous, crack-free coatings with uniform nanoscale roughness (5-fold lower variability) and enhanced wettability (initial contact angle 40° vs. 82°), establishing dense WO_3/Ni interfacial contacts that were not achievable for WO_3-C-PBM. Electrochemically, WO_3-S-PBM/Ni delivered a current density of 84.8 mA cm^{-2} at 1.65 V vs. RHE with 328 mV

overpotential a 3-fold enhancement over WO_3-C-PBM (375 mV) despite nearly identical active surface areas (<3% difference). Cyclic voltammetry demonstrates that this superior performance arises from phase-selective stabilization of the intrinsically more active γ-NiOOH (1.45 V vs. RHE) at uniform WO_3-S-PBM interfaces, whereas heterogeneous WO_3-C-PBM coatings permit mixed β/γ phase coexistence. These results establish the interplay of extrinsic mechanochemical activation with intrinsic phase and crystallinity as a critical, previously overlooked design parameter governing interfacial phase selectivity and OER activity in metal-oxide composite electrocatalysts.

1. Introduction

Alkaline water electrolysis is widely regarded as a key technology for large-scale, carbon-neutral hydrogen production, yet its overall efficiency is still limited by the sluggish kinetics of the oxygen evolution reaction (OER) at the anode [1-3]. Because OER proceeds through multiple proton-coupled electron-transfer steps and the formation of an O-O bond, substantial overpotentials are typically required, which directly increases the energy cost of hydrogen generation [4, 5]. Consequently, there is a continuing drive to develop electrocatalysts that combine high OER activity with long-term stability under strongly oxidizing alkaline conditions, while relying on earth-abundant elements suitable for scale-up [6-8].

Benchmark OER catalysts in acidic media are based on Ir and Ru oxides, which offer outstanding activity but suffer from scarcity, high cost, and limited durability in alkaline environments [8, 9]. This has stimulated intensive research on non-precious transition-metal systems, particularly Ni-, Co-, Fe- and Mn-based (oxy)hydroxides and their mixed compositions which can display excellent alkaline OER performance when composition, defect chemistry, and nanostructure are carefully tuned [10, 11]. However, these materials can still undergo phase transformations, partial dissolution, or conductivity limitations at high current densities, and their performance is often sensitive to subtle changes in electrode architecture and support [6, 12-14]. Identifying alternative oxide platforms with complementary stability, electronic tunability, and well-defined structure-activity relationships therefore remains an important goal.

Tungsten trioxide (WO_3) is an attractive candidate in this context. It is composed of relatively abundant elements and is well known for its high corrosion resistance in oxidizing aqueous environments, including harsh acidic solutions, which suggests that it could also act as a robust matrix under alkaline OER conditions [15-18]. WO_3 is an n-type semiconductor with a band

gap of roughly 2.5-3.0 eV and a rich polymorphism arising from corner-sharing WO_6 octahedra. Its electronic structure can be tuned through phase selection, stoichiometry control, and oxygen-vacancy engineering [19-21]. These features have underpinned its extensive deployment in gas sensors, electrochromic devices, and photo- and electrocatalytic water-splitting applications, where WO_3 frequently serves as a functional scaffold or support for more active phases. Recent studies on WO_3-based films, nanoarrays, and defect-engineered WO_{3-x} have demonstrated that the activity of tungsten oxides can be substantially enhanced by controlling thickness, morphology, and defect density, and that interfacial coupling with metals or other oxides can further boost OER performance [22-24].

Despite recent advances in understanding WO_3 electrochemistry, fundamental questions remain regarding its intrinsic OER activity in alkaline media, especially for powder catalysts and thin films on metallic supports relevant to practical devices. Most prior investigations either focus on WO_3 as a photoanode in neutral or mildly basic electrolytes or embed it in composite electrodes where the contribution of WO_3 is convoluted with that of co-catalysts, conductive additives, and complex morphologies [25-27]. However, far less attention has been given to how precursor structural quality specifically, commercial polycrystalline powder versus synthesized single-crystal WO_3 [28], together with mechanochemical activation, influences the defect landscape and Ni/WO_3 interfacial properties. While both materials can exhibit comparable particle sizes after processing, synthesized single-crystal WO_3 (grown via physical vapor transport) offers well-defined crystallographic structure and equilibrated growth history, whereas commercial powders reflect industrial synthesis routes with less controlled crystallization conditions, which may influence dispersion, coating uniformity, and interfacial contact. Mechanochemical activation via planetary ball milling (PBM) is known as a scalable method to nanostructure materials and tune surface chemistry, yet how processing history for different feed powders propagates through electrode fabrication to govern metal-semiconductor junction properties remains unexplored. Since interfacial electronic structure between catalyst layer and metal substrate is known to play a decisive role in OER kinetics, clarifying how crystal origin and mechanochemical processing couple to determine catalytic activity is essential for establishing WO_3 as an active, noble-metal-free anode material in alkaline water electrolysis.

In this work, monoclinic WO_3 is employed as a model system to address these questions through systematic comparison of commercial polycrystalline, WO_3-C versus synthesized single-crystal, WO_3-S and their impact on Ni/WO_3 interfacial electrochemistry. Both materials are subjected to mechanochemical activation to generate processable nanoscale powders, formulated into stable inks via Hansen solubility parameter mapping, and deposited as catalyst

layers on Ni substrates for alkaline OER evaluation. By directly comparing the structural evolution, surface chemistry, electrode morphology, and electrochemical behavior of ball-milled commercial WO_3-C-PBM versus synthesized WO_3-S-PBM, this study elucidates how precursor crystal origin through its influence on particle fragmentation, defect reorganization, and coating uniformity governs WO_3/Ni interfacial properties and subsequent nickel oxyhydroxide phase selectivity, the true determinant of alkaline OER activity.

2. Materials and Methods

2.1. Materials and Processing

WO_3-C powder (Sigma-Aldrich, 99.5% purity) and single-crystalline WO_3-S by a physical vapor transport (PVT) method were used as starting materials. The synthesis and detailed characterization of the WO_3 single crystals have been reported previously [28]. In the present work, both the commercial powder and the PVT-grown WO_3 were employed as feed materials for particle size reduction via PBM. Prior to milling, the synthesized WO_3 crystals, obtained as bulk chunks, were manually ground using an agate mortar and pestle to break them into smaller fragments suitable for milling.

PBM experiments were performed using a planetary ball mill (Retsch PM 100). Identical milling conditions were applied to both WO_3 materials, the commercial powder and the PVT-synthesized and mortared single crystals throughout this study. A total of 312.5 mg of WO_3 feed material was mixed with 46.9 g of yttria-stabilized zirconia (YSZ) beads, corresponding to a fixed powder-to-beads mass ratio of 1:150. Owing to the relatively large size of the WO_3 crystal fragments, beads with a diameter of 0.3 mm were used. Milli-Q water (resistivity of 18.2 MΩ cm) was added as a process control agent in an amount of 2 μL mg^{-1} relative to the catalyst powder. Milling was carried out in a 50 mL zirconia milling jar at a rotational speed of 400 rpm for a total duration of 2 h. To control temperature increases during milling, milling was stopped for 1 min between cycles, providing a passive cooling interval without active temperature control. During operation, a maximum temperature of approximately 50 °C was recorded at the outlet. To ensure homogeneous mixing and efficient grinding, the rotational direction was alternated between clockwise and anticlockwise every 30 min. After PBM, the resulting suspension was flushed out of the milling jar using Milli-Q water. The collected material was subsequently dried in a vacuum oven at 60 °C for 20 h to ensure complete removal of residual moisture. The resulting milled materials are hereafter referred to according to their respective feed material origins, WO_3-C, WO_3-S, WO_3-C-PBM and WO_3-S-PBM [29].

2.2.Characterization methods

The WO_3 powders and drop-cast coatings were characterized using a range of analytical techniques, with full experimental details provided in the Supplementary Information (SI. Section 2). Further details of the ink formulation procedure, including representative images, are given in (SI. section 1.2, Figure **S5**).

3. Results and Discussion

Figure 1. illustrates the material processing strategy employed in this study. Both commercial and single-crystal WO_3 samples exhibited excessively large particle sizes that precluded their direct use in electrode fabrication for OER applications. Attempts to formulate stable ink dispersions from the as-received materials proved unsuccessful, as the large particles could not be effectively dispersed even under intensive ultrasonication. This challenge-commonly encountered with as-supplied metal oxide powders [29, 30]-necessitated a particle size reduction strategy to achieve processable materials suitable for electrode preparation.

To address this fundamental limitation, we implemented mechanochemical treatment by planetary ball milling previously established for NiO-based electrocatalysts [29] for both samples, WO_3-C and WO_3-S (for details see Chapter 2). In the following, we will focus on the thereby induced structural, morphological, and physicochemical transformations, including particle size distribution, crystallographic evolution, defect chemistry, surface properties, and dispersion stability behavior.

To correlate material modifications with functional performance, drop-casted electrodes were prepared on Ni substrates for electrochemical evaluation. While electrode fabrication was deliberately kept simple to isolate material-property effects, the OER testing provided critical validation of whether mechanochemical processing could successfully transform these large-particle WO_3 materials into viable electrocatalysts. This integrated approach-combining, detailed characterization of powder properties with the testing of the powder's electrochemical performance to assess functionality, enables elucidating structure-property-performance relationships.

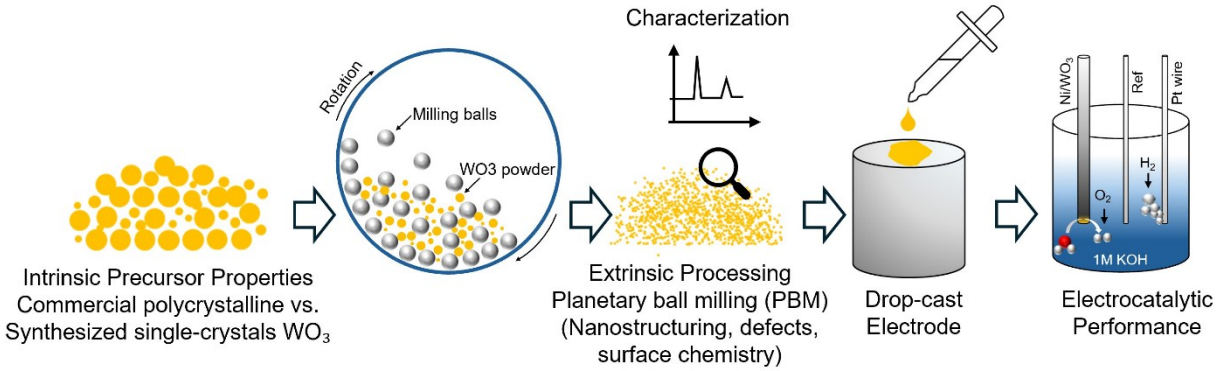

Figure 1. The schematic illustrates the experimental rationale, progressing from bulk WO_3 with defined intrinsic crystallinity and phase, through defect-rich nanoscale WO_3 generated by planetary ball milling, to electrode fabrication and OER functionality governed by Ni-WO_3 interfacial properties.

3.1. Particle morphology, structure, and composition analysis

Transmission electron microscopy with energy dispersive X-ray spectroscopy (TEM-EDX) was employed to evaluate the morphology of all the WO_3 specimens. These are WO_3-C and WO_3-S feed powders, and WO_3-C-PBM and WO_3-S-PBM particles after PBM. **Figure 2** shows representative TEM images together with the respective selected area electron diffraction (SAED) patterns and high-resolution TEM (HR-TEM) images. The commercial WO_3-C (a) comprises large faceted agglomerates (≈430 nm. Ball milling (WO_3-C-PBM, d) of this powder resulted in loosely aggregated smaller crystallites (few tens of nm), exposing high-index facets that enhance charge transfer. In contrast, the WO_3-S after (g) exhibits well-defined single-crystals (≈373 nm) with pristine surfaces, whereas subsequent post-PBM sample (WO_3-S-PBM, j) shows finer, more homogeneous nanocrystals (≈20-50 nm).

All SAED patterns confirm a polycrystalline character of all samples. Indexed rings denoted by (020) and (200) planes match the monoclinic γ-WO_3 phase (d-spacings ≈3.77 Å and ≈3.74 Å), that is preserved across samples, even after PBM. HR-TEM across all variants displays identical lattice fringes with interplanar spacings of ≈2.7 Å and ≈1.3 Å, respectively for the (200) and (400) planes, corroborating uniform monoclinic WO_3 phase.

EDX compositional analysis reveals precursor-specific elemental signatures that persist through ball milling (**Figure S1**). EDX analysis of the commercial WO_3-C before PBM detected higher amount of W than expected (66.8 at% O and 33.2 at% W) thus deviating from the nominal composition. 66.8 at% O and W. Single-crystal WO_3-S exhibits O (74 at%), W (24.5 at%) thus yielding near stochiometric composition with trace C, Co, and K impurities from

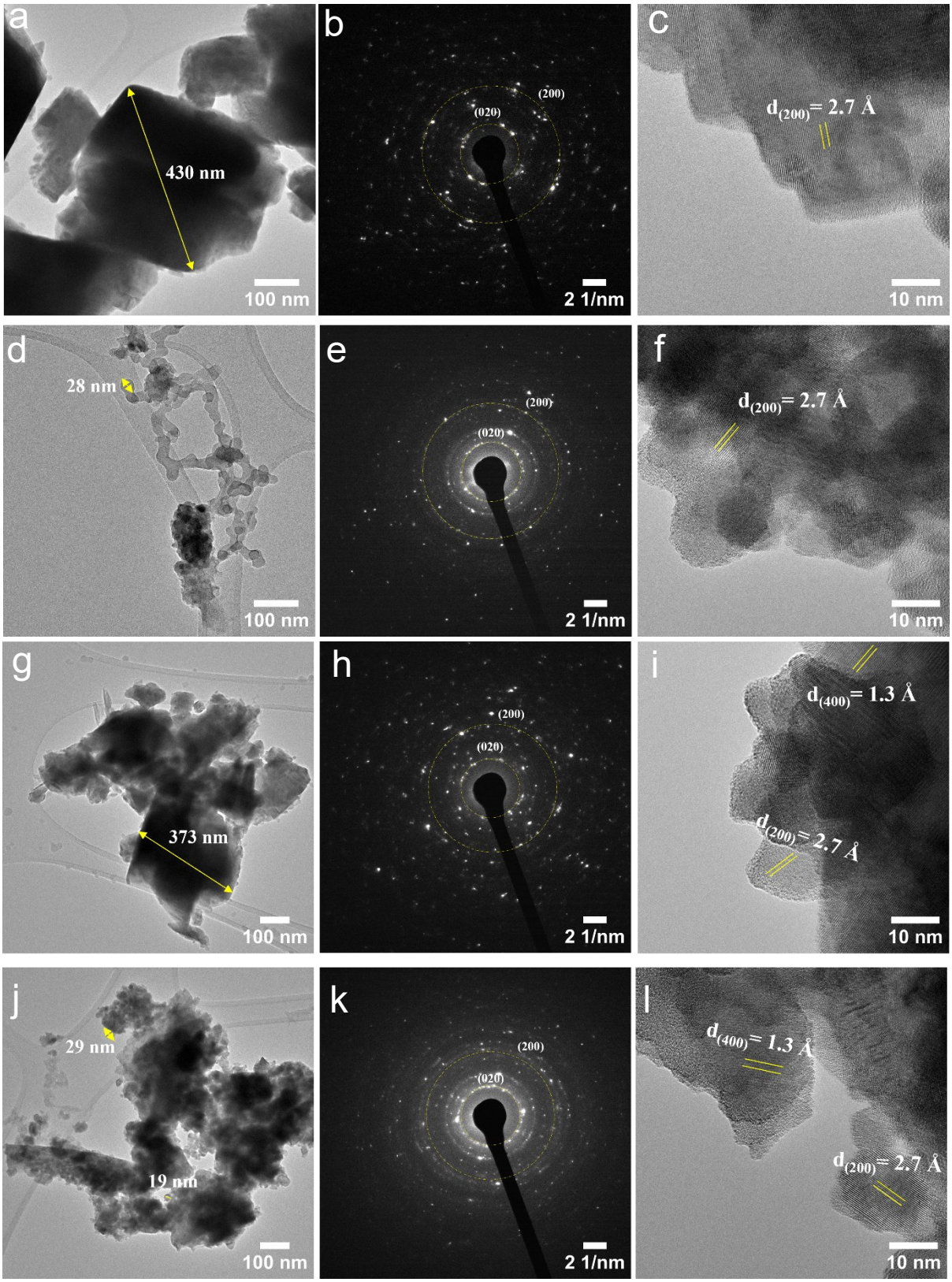

Figure 2. Assessment of the samples' morphology. TEM images of (a) WO_3-C (d) WO_3-C- PBM (g) WO_3-S and (j) WO_3-C- PBM and SAED patterns of (b) WO_3-C (e) WO_3-C- PBM (h) WO_3-S and (k) WO_3-S-PBM, showing the monoclinic structure with selected crystal reflections marked; HR-TEM image of a crystalline particle with the measured interplanar spacing marked for of (c) WO_3-C (f) WO_3-C- PBM (i) WO_3-S and (l) WO_3-S- PBM.

synthesis. After PBM, WO_3-C-PBM displays O (77 at%), W (20 at%) including minor Ca and K, while WO_3-S-PBM shows comparable O/W ratios with similar trace contaminants. The observed deviations in the W:O ratios between the pre- and post-PBM samples likely originated from the presence of hydroxylation groups after PBM.

The local structure of the bulk and ball milled samples was investigated using synchrotron total scattering with analysis of the atomic pair distribution function (PDF), shown in **Figure 3**. All samples exhibit very similar PDF in a real space range up to r = 30 Å, indicating a similar local structure. Beyond this range (r > 40 Å), a clear variation in the atomic pair correlations between commercial and synthesized bulk WO_3 powders is observed and attributed to differences in the long range structure. The two relevant crystal phases for WO_3 at ambient temperatures are monoclinic γ- and triclinic δ-WO_3 [31].

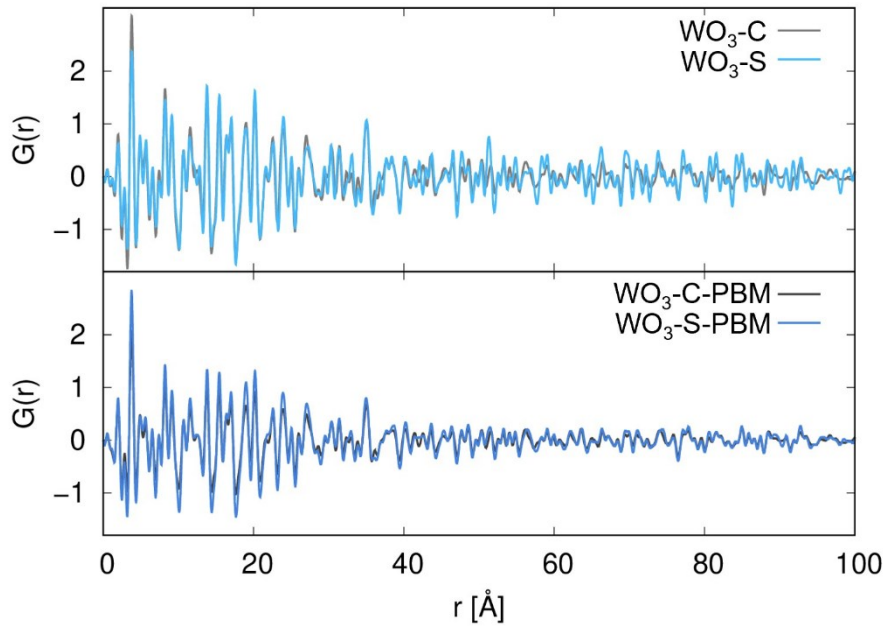

Figure 3: Assessment of the samples' structure by synchrotron total scattering with analysis of the atomic pair distribution function. Pair distribution function G(r) of pristine (top) and ball-milled (bottom) WO_3, showing similarities in the short-range correlations and differences in the long-range order that converge after mechanochemical treatment].

Calculated PDF for these phases (SI) suggest that the local structure up to r = 30 Å is very similar, whereas clear deviations are found in a higher r range that enable phase analysis from PDF data at r > 40 Å. PDF refinements over 40 Å < r < 70 Å **(Figure S3**, **S4 and ST2**) reveal WO_3-S contains 52(5) % γ-WO_3 and 48(5) % δ-WO_3, in excellent agreement with Rietveld analysis [28], while WO_3-C contains 27(6) % γ-WO_3 and 73(6) % δ-WO_3 a significantly higher triclinic fraction.

Upon ball milling, the PDF profiles converge remarkably across the entire r range. Phase analysis yields 40(7)% γ-WO_3 / 60(7)% δ-WO_3 for WO_3-S-PBM and 28(10)% γ-WO_3 / 72(10)% δ-WO_3 for WO_3-C-PBM. Ball milling thus induces partial γ→δ phase transformation in WO_3-S (52 % → 40 % monoclinic), likely through mechanochemical strain accumulation, while WO_3-C remains phase-stable (27 % → 28 %, within error). This results in partial convergence of phase compositions, though a 12 % difference persists.. The observed PDF convergence at medium-to-long range arises from uniform nanocrystallite formation (20–50 nm, TEM-confirmed) with similar coherence lengths and grain boundary structures, rather than complete phase equilibration. Critically, local WO_6 octahedral coordination (r < 10 Å) remains intact, demonstrating that mechanochemical processing by PBM modifies crystallographic registry without disrupting fundamental W-O bonding.

Raman spectroscopy (**Figure 4**) provides complementary vibrational evidence for monoclinic phase preservation, as well as the phase homogenization after the ball-milling process. All spectra display similar yet non-identical peak positions spanning lattice modes (<220 cm^{-1}), O-W-O bending (220-580 cm^{-1}) and stretching modes (650-900 cm^{-1}), with signature 770-820 cm^{-1} bands assigned to terminal W=O/bridging W-O-W linkages [32, 33]. While all materials display characteristic γ monoclinic phase peaks around 274, 719, and 808 cm^{-1} [28, 34], confirming retention of the monoclinic phase component. This is consistent with the PDF

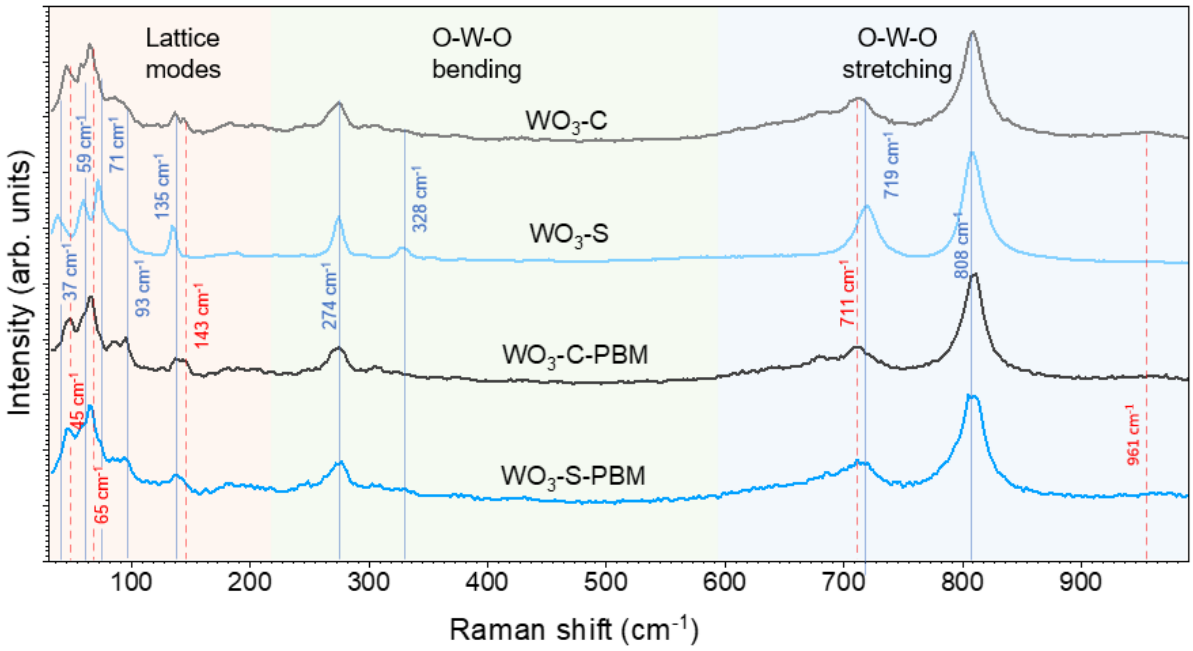

Figure 4: Assessment of the samples' structure by Raman spectorscopy. Raman spectra of WO_3-C, and WO_3-S, in pristine and PBM states. Blue lines indicate characteristic vibrational modes of WO_3-S. Red dashed lines depict the deviations of the WO_3-S, vibrational modes.

quantification (28-40% γ-WO_3 in milled samples). However, Raman cannot reliably quantify phase fractions due to overlapping δ-triclinic contributions.

Raman peaks of WO_3-S-PBM exhibit systematic broadening compared to those taken of WO_3-S before PBM. This is most evident in the W-O-W bending and stretching regions, directly reflecting the TEM-confirmed crystallites refinement from ~ 400 nm to 20-50 nm. In the case of WO_3-C, the polycrystalline nature of the powder already leads to a broadened Raman spectrum before PBM, which notably does not differ greatly after the mechanochemical treatment. Furthermore, both WO_3-S and WO_3-S-PBM mainly shows a different set of lattice modes at 37, 59, 71, 93, and 135 cm^{-1}. These low frequency lattice modes are usually attributed to defects, strain, and the collective relations of the WO_6 octahedral units [35, 36], and they appear to be almost identical for both samples with peaks at 45, 65, 71, 135, and 143 cm^{-1}. This demonstrates that mechanochemical processing homogenizes the local structural environment defect density, strain distribution, and grain boundary character even though bulk phase fractions retain a 12% difference (PDF).

Figure 5, shows FTIR spectra of WO_3 precursors and their ball-milled counterparts in the 400-4000 cm^{-1} range, highlighting changes in the O-H content as a function of PBM and precursor type. FTIR spectroscopy was employed to probe how feed and PBM samples affect the local bonding environment and surface hydroxylation of WO_3 [37]. The spectra of all samples are dominated by intense bands at 630 and 820 cm^{-1}, which are assigned to W-O-W and O-W-O lattice vibrations of monoclinic WO_3 and confirm that the fundamental oxide phase is preserved upon ball milling. In the mid-infrared region, weak features around 1600-1700 cm^{-1} are attributed to C═C/C═O stretching of adventitious carbonaceous species.

A broad band in the 3200-3600 cm^{-1} region is observed for all samples and is assigned to O-H stretching modes of surface hydroxyl groups and hydrogen-bonded water [38]. Notably, this O-H band is markedly more intense for WO_3-S-PBM than for the commercial and non-milled counterparts, indicating a substantially higher density of surface hydroxyls and/or more strongly bound water on the ball milled single crystal derived WO_3 (Table **ST1**). Relative O-H content follows the order: WO_3-S-PBM > WO_3-C-PBM > WO_3-S > WO_3-C.

This enhancement is consistent with the generation of additional surface defects and nanostructuring during high-energy milling, which increases the population of coordinatively unsaturated W sites capable of binding -OH and H_2O. The pronounced O-H signature of WO_3-S-PBM points to a more strongly hydrated, hydroxyl-rich surface, which is expected to

promote favorable interactions with electrolyte. The mechanochemical fragmentation process exposes fresh, reactive bulk interiors while simultaneously removing surface contamination, creating a clean, hydroxyl-rich surface. The WO_3-S-PBM, fragmenting more uniformly into discrete 20-30 nm nanoparticles (TEM), achieves higher surface area compared to the WO_3-C-PBM, which yields larger, more aggregated structures with less accessible surface area. Raman spectroscopy corroborates this interpretation: post-milling peak broadening in the bending and stretching regions reflects the formation of nanocrystallites, while the convergence of low-frequency lattice modes indicates similar local structural environments in both ball-milled samples despite their different precursor origins. Combined with synchrotron total scattering data evidencing medium-range structural homogenization and preserved WO_6 connectivity, these FTIR data establish that mechanochemical processing of single-crystal WO_3 enhances surface hydroxylation through controlled nanostructuring while maintaining the fundamental WO_3 framework. [39].

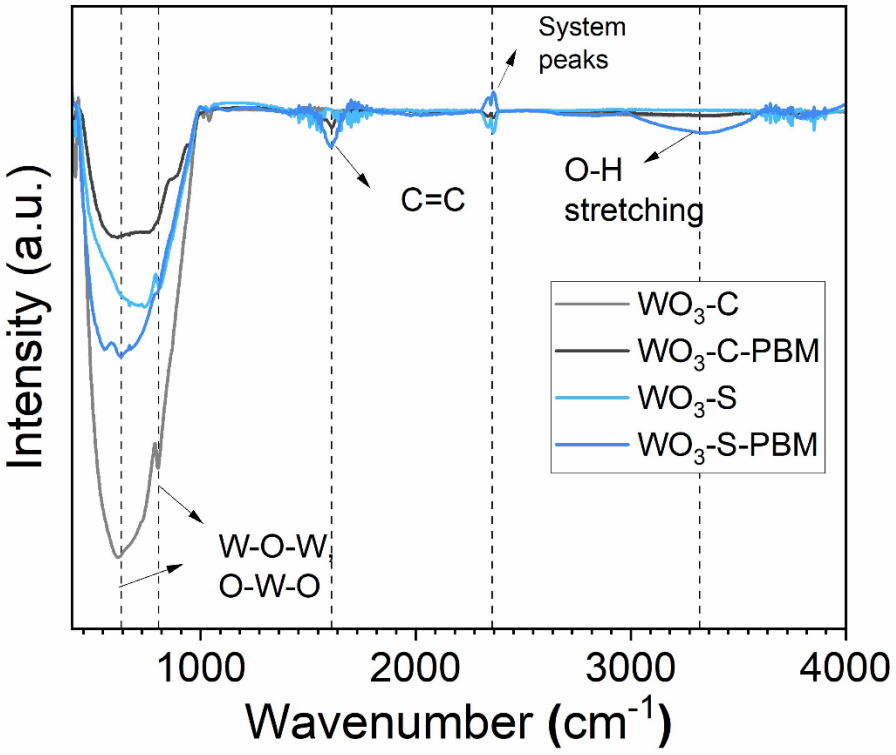

Figure 5. FTIR analysis of vibrational modes and surface species. FTIR analysis of WO_3 of commercial- and single-crystal-derived WO_3 before and after ball milling, showing enhanced O-H stretching for WO_3-S-PBM.

XPS was employed to assess how PBM and crystal origin influence WO_3 surface chemistry. Survey spectra (**Figure S2**) of all samples exhibit identical W 4f doublet positions, confirming a dominant W^{6+} oxidation state and a consistent WO_3 phase across synthesized, commercial,

and ball-milled materials. High-resolution C 1s spectra show that WO_3-C exhibits lower surface carbon contamination, whereas WO_3-S displays a higher C 1s intensity. Upon PBM, the C 1s intensity of WO_3-S-PBM is reduced to a level comparable to that of WO_3-C-PBM, indicating effective removal of adventitious carbon contamination through the mechanochemical ball-milling process. At the same time, the W 4f and O 1s peak positions remain essentially unchanged upon milling, demonstrating that the electronic structure of WO_3 is largely preserved.

Deconvolution of the W 4f region shows that all samples feature main W $4f_{7/2}$ and W $4f_{5/2}$ components at approximately 36.2 and 38.3 eV, respectively, characteristic of W^{6+} in stoichiometric monoclinic WO_3 and in agreement with literature reports for crystalline WO_3 powders (**Figure 6**). In the synthesized material, WO_3-C and WO_3-S, before PBM, a weak lower-binding-energy contribution can be fitted and assigned to W^{5+} species associated with sub-stoichiometric WO_3 or surface oxygen vacancies, as commonly observed in defect-engineered WO_3 systems [40, 41]. After ball milling, the W^{5+} component is strongly attenuated and the W 4f envelope becomes dominated by the W^{6+} doublet, indicating suppression of surface oxygen vacancy defects. This surface oxidation occurs through mechanochemical exposure of stoichiometric bulk interiors during particle fragmentation, as evidenced by reduced C 1s contamination and enhanced surface hydroxylation observed by FTIR. However, this surface renewal occurs alongside, not in contradiction to, the introduction of bulk structural disorder: Raman peak broadening reflects nanosizing-induced phonon

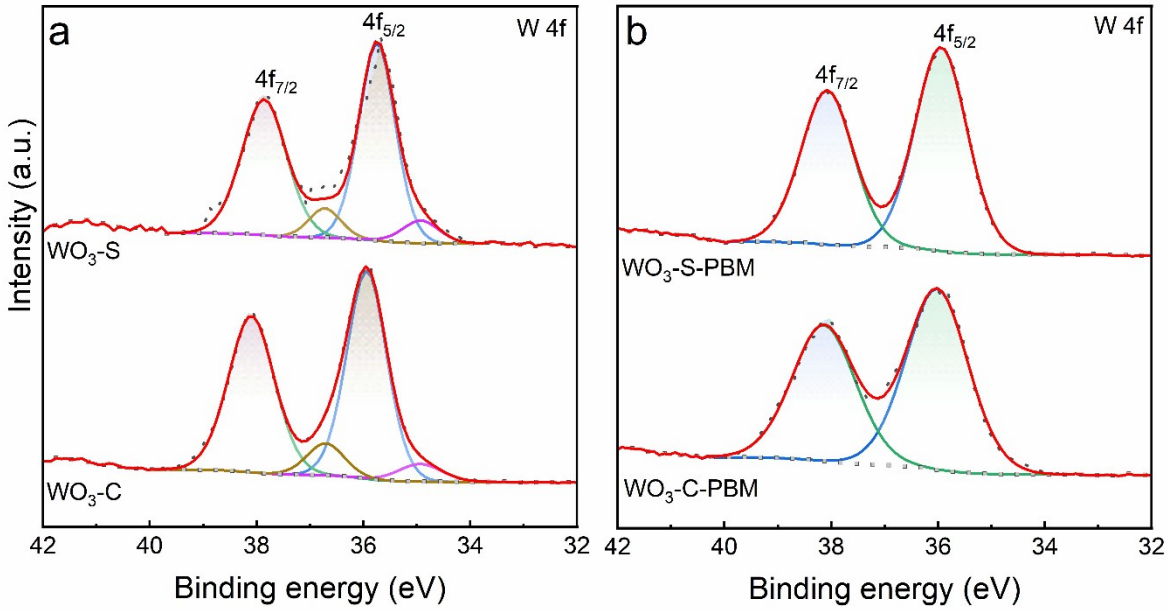

Figure 6. Assessment of the samples' surface chemical states by XPS. High-resolution XPS W 4f spectra of WO_3 (a) before and (b) after ball milling, highlighting changes in surface defects and contamination.

confinement with convergence of low-frequency lattice modes, while synchrotron analysis confirms medium-range structural homogenization and partial γ→δ phase transformation in WO_3-S (52 % → 40 % monoclinic). Critically, the W^{6+} electronic structure remains unchanged (XPS) since both γ- and δ-polymorphs contain W^{6+} in similar octahedral coordination. The observed phase transformation alters crystallographic registry, not local oxidation state.

Thus, mechanochemical activation achieves a dual effect: (1) surface cleaning and stoichiometric renewal (suppression of W^{5+} oxygen vacancy defects and removal of carbon contamination, creating hydroxyl-rich W^{6+} surfaces), and (2) beneficial bulk nanostructuring with partial phase redistribution. This establishes a well-defined model system where the superimposed effects of precursor crystal quality, mechanochemical processing, and resulting material architecture can be systematically disentangled. Precursor-dependent differences in phase composition (40% vs. 28% γ-WO_3) and morphology become key determinants of subsequent ink formulation, electrode fabrication, and OER performance.

3.2. Physicochemical assessment via liquid phase interaction

Besides understanding powder properties, the powders' behavior in liquid can shed light on their physicochemical properties. In particular, when processing occurs via the liquid phase during dispersion, coating and drying. This will be discussed in the following.

3.2.1. Dispersibility by Hansen solubility parameters

In a first step, understanding the intricate relationship between probe liquids with known polarity and catalyst materials is crucial since liquids are used to transport catalyst materials throughout the coating and drying process. After thoroughly characterizing the WO_3-C-PBM and WO_3-S-PBM powders in the dry state, we analyzed the powder-liquid interaction with probe liquids of known polarity to assess the particles' surface properties in terms of their HSPs.

According to HSP theory, the three parameters from dispersion forces (δD), dipolar intermolecular force (δP), and hydrogen bonds (δH) between probe liquids and catalyst particles can be represented as coordinates in the three-dimensional Hansen space [42, 43]. In line with our previous works [44], we used the two-step procedure of Amin et al. to select the appropriate probe liquids for determining HSP of WO_3-C-PBM and WO_3-S-PBM powders. In the first step, the interaction of the material with the three initial probe liquids of different protic behavior namely – EtOH (protic polar), DMF (aprotic polar), THF (moderate polar) is observed. Based on which probe liquids in the first step formed sedimentation-stable dispersions or not, further probe liquids were added accordingly to define the final probe liquid list for determining HSP.

In case of WO_3-C-PBM and WO_3-S-PBM powders, in the first step, all three initial probe liquids namely EtOH, DMF, and THF, enabled stable dispersions with both powders. This meant that the material interacted well with all protic polar and aprotic polar probe liquids. Hence, in the second step, IPA (protic polar), DMSO (aprotic polar), NMP (aprotic polar), and PC (aprotic polar) were added. The relative sedimentation times, determined from the evolution of the integral extinction of the sedimenting dispersions, were used to rank these eight probe liquids from the best to the least compatible solvent (details in SI 2.10). HSPiP software was used to calculate HSP of the material using the automated-addition-method developed by Süß et al. [45]. The resulting HSP of WO_3-C-PBM and WO_3-S-PBM and its HSP sphere are shown in **Figure 7**.

a

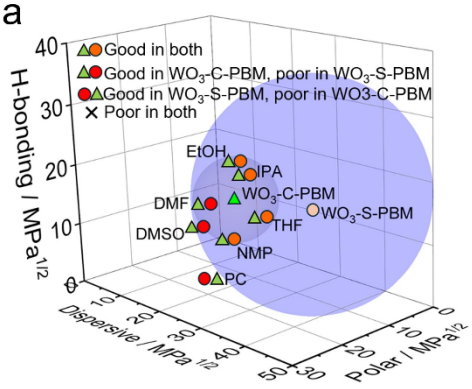

b

Material	WO_3-C-PBM	WO_3-S-PBM
Disperse interactions δ_D ($MPa^{1/2}$)	*16.92*	*24.15*
Polar interactions δ_P ($MPa^{1/2}$)	*10.65*	*0.42*
Hydrogen bonding δ_H ($MPa^{1/2}$)	*13.02*	*12.96*
Sphere radius r ($MPa^{1/2}$)	*7.1*	*19.9*
Outliers	*0*	*0*
Fitting	*1*	*1*

Figure 7. HSP determination of WO_3-C-PBM and WO_3-S-PBM with the categorized probe liquids. (a) HSP sphere and indication of probe liquids for WO_3-C-PBM and WO_3-S-PBM and (b) HSP coordinates as table.

From the HSP it becomes clear that the two materials are clearly distinct from each other. WO_3-C-PBM has a significantly lower disperse (δD) and a much higher polar contribution (δP) than WO_3-S-PBM. The hydrogen bonding (δH) remains rather constant because δH reflects the effective hydrogen-bonding interactions governing dispersion behavior rather than the absolute concentration of surface -OH groups. For metal oxides, additional hydroxylation often leads to saturation of accessible hydrogen-bonding sites or the formation of strongly bound hydroxyl/water species that do not significantly alter solvent-surface interactions in organic media [46].

3.3. Layer property assessment

To evaluate the electrode surface characteristics in detail, SEM and AFM analyses were performed on WO_3-drop casted Ni substrates. Their combination reveals the interplay between

coating morphology, particle distribution, and surface topography for the two WO_3 precursor-derived electrodes after drop-casting and drying.

3.3.1. Morphology analysis of drop-casted layers

SEM investigations provide information on the microstructure (**Figure 8 a,b**). They reveal distinctly different surface morphologies for the commercial-derived and single-crystal-derived ball milled electrodes. The WO_3-C-PBM electrode (Figure 8a) displays a heterogeneous morphology characterized by loosely aggregated clusters and isolated larger particles scattered across the Ni substrate. The inset reveals distinct aggregates with irregular morphology and visible interparticle voids, indicating poor packing efficiency. In contrast, the WO_3-S-PBM electrode (Figure 8b) exhibits a continuous, homogeneous coating with fine nanoparticles uniformly distributed across the surface. The inset shows densely packed particles forming a crack-free film with minimal void space. These SEM micrographs indicate that the two feeds, despite undergoing identical PBM and ink formulation procedures, yield fundamentally different coating architectures due to their distinct fragmentation and reaggregation behavior.

Subsequently, AFM-MSDQ was employed to quantify surface topography over 100 × 100 μm² regions. Figure 8 c,d show the surface height distributions of the WO_3-C-PBM and WO_3-S-PBM electrodes, respectively (Parameters utilized in MSDQ are given in Table **ST3**). Evaluating the entire scan area, the WO_3-C-PBM electrode (Figure 8c) exhibits a surface roughness of 288.16 ± 172.72 nm with a homogeneity score of 0.868 ± 0.122 and a roughness factor of 1.113 ± 0.058. The exceptionally large standard deviation in surface roughness (±172.72 nm) and low homogeneity score directly reflect the heterogeneous coating quality observed in SEM. The topographical analysis reveals pronounced spatial variability, with multiple large, isolated features (red/yellow/orange) corresponding to aggregates or particle clusters (marked with red circles). Notably, three major aggregate clusters are visible, with the largest reaching heights of 4-5 μm. The predominance of dark blue regions with scattered green spots indicates extensive areas with minimal WO_3 coverage interspersed with moderate-height features, creating a patchy, non-continuous coating. The relatively low roughness factor (1.113), despite high absolute roughness suggests that the surface area enhancement is limited by poor particle distribution.

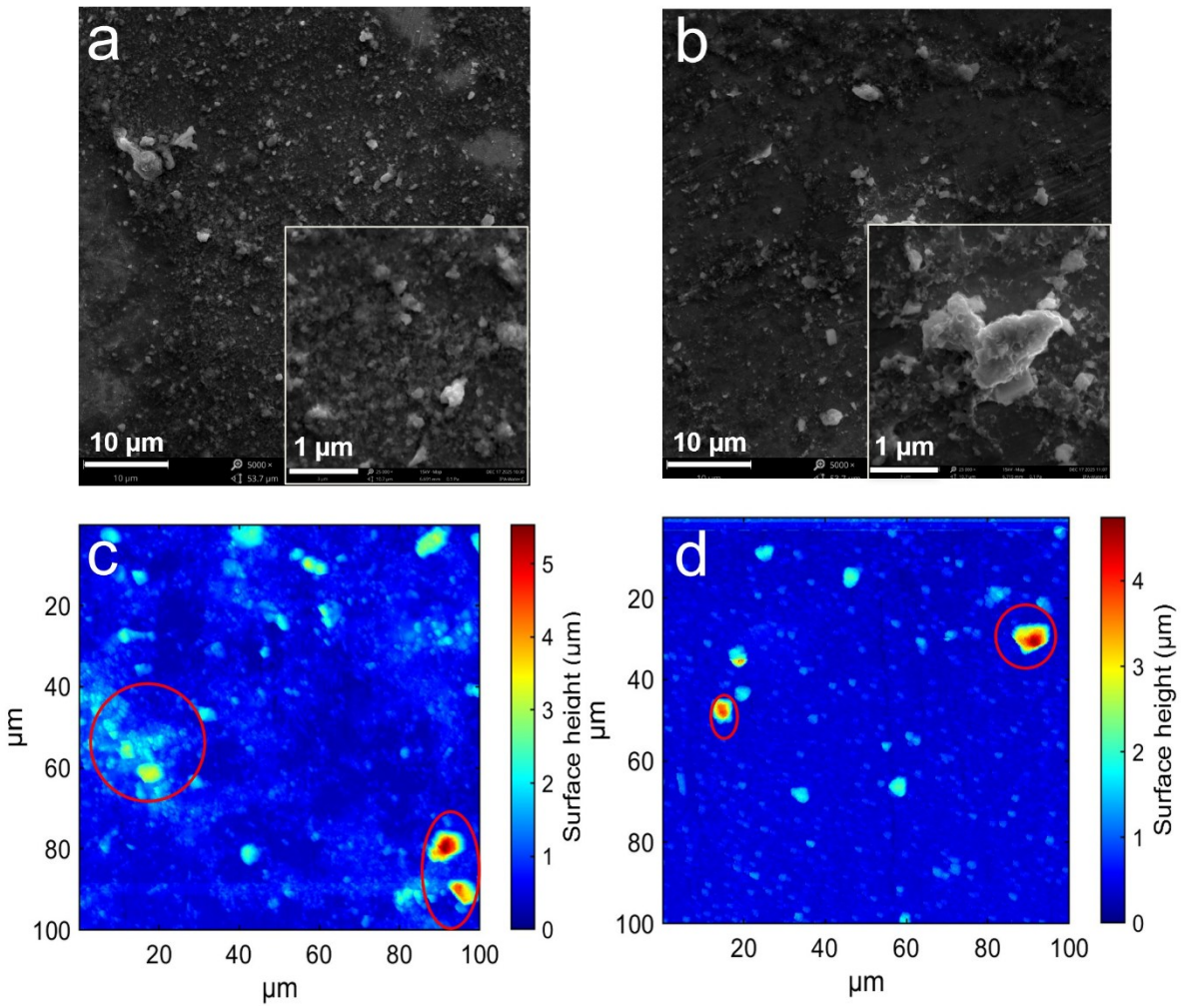

Figure 8. SEM and AFM surface analysis of ball-milled WO_3-coated Ni electrodes. SEM secondary electron micrographs of (a) WO_3-C-PBM and (b) WO_3-S-PBM electrodes with insets showing higher magnification, and corresponding AFM topographical maps of (c) WO_3-C-PBM and (d) WO_3-S-PBM over 100 × 100 µm² areas. Red circles highlight isolated aggregates. Scale bars represent surface height from (c) 0 to 5.2 µm and (d) 0 to 4.5 µm.

In contrast, the WO_3-S-PBM electrode (Figure 8d) exhibits a surface roughness of 268.49 ± 32.87 nm with a homogeneity score of 0.909 ± 0.070 and a roughness factor of 1.283 ± 0.109. Critically, while the average roughness values are comparable between the two samples (288 vs. 268 nm), the standard deviation for WO_3-S-PBM is more than 5-fold lower (±32.87 vs. ±172.72 nm), indicating a substantially more uniform surface topology. The higher homogeneity score (0.909 vs. 0.868) and elevated roughness factor (1.283 vs. 1.113) confirm that WO_3-S-PBM achieves controlled nanoscale roughness distributed more homogeneously over the substrate. While two isolated features are present (marked with red circles, reaching ~4 µm height), they are significantly fewer in number compared to WO_3-C-PBM, and the overall surface exhibits more uniform blue-cyan coloration, indicating consistent baseline

coverage with controlled moderate roughness rather than the extreme height variations and extensive void areas characteristic of WO_3-C-PBM.

This combined SEM-AFM analysis demonstrates that precursor crystal origin fundamentally determines electrode-scale morphology despite identical processing conditions. The WO_3-S-PBM coating achieves superior spatial uniformity evidenced by 5-fold lower roughness variability (±32.87 vs. ±172.72 nm), 5 % higher homogeneity score (0.909 vs. 0.868), and significantly fewer large aggregates (2 vs. 3+ major features) with more continuous baseline coverage and beneficial nanoscale texturing (roughness factor 1.283). This uniform nanostructured architecture creates dense WO_3/Ni interfacial contact over most of the electrode area, establishing consistent interfacial properties across the electrode surface. Conversely, the WO_3-C-BM coating exhibits macroscopic heterogeneity with comparable average roughness but extreme spatial variability (±172.72 nm standard deviation) arising from numerous isolated aggregates rather than controlled nanostructuring. This non-uniform morphology, characterized by a low roughness factor (1.113) and poor homogeneity score (0.868), results in incomplete substrate coverage with spatially heterogeneous WO_3/Ni interfacial regions: some areas with dense oxide coverage and others with exposed or poorly covered Ni surface.

3.3.2. Wettability and ink drying behavior

Contact angle and evaporation temperature measurements were performed to evaluate ink drying behavior and surface wettability, both critical factors influencing final electrode morphology [11]. **Figure 9a** presents temperature profiles during ink droplet evaporation on Ni substrates heated to 50 °C, with representative thermal imaging snapshots at initial and final drying stages, while Figure 9b shows time-dependent contact angle evolution for water droplets on WO_3-coated electrodes. Wettability is particularly important for OER electrodes because oxygen bubbles continuously form and detach from the catalyst surface during operation, requiring rapid rewetting of the freshly exposed surface with electrolyte. This repetitive wetting-dewetting cycle makes the initial contact angle and wetting kinetics more decisive for sustained catalytic performance.

The radiant temperature measurements using infrared camera during ink droplet evaporation provide mechanistic insight into how these surface properties translate to coating formation (Figure 9a). Both samples undergo evaporative cooling as solvent evaporates, but with markedly different kinetics. WO_3-C-PBM shows slower, more gradual cooling, reaching its temperature minimum (~23.6 °C) only after ~40 seconds, followed by protracted rewarming.

In line with the coating heterogeneity discussed in the previous section, this extended thermal profile indicates spatially variable evaporation rates and non-uniform drying behavior. In contrast, WO_3-S-PBM exhibits rapid temperature decrease to a minimum of ~23.4 °C within 20 seconds, followed by swift rewarming to ambient temperature. Inline with the coating homogeneity discussed in the previous section, this extended thermal profile points towards heterogeneous drying with spatially variable evaporation rates.

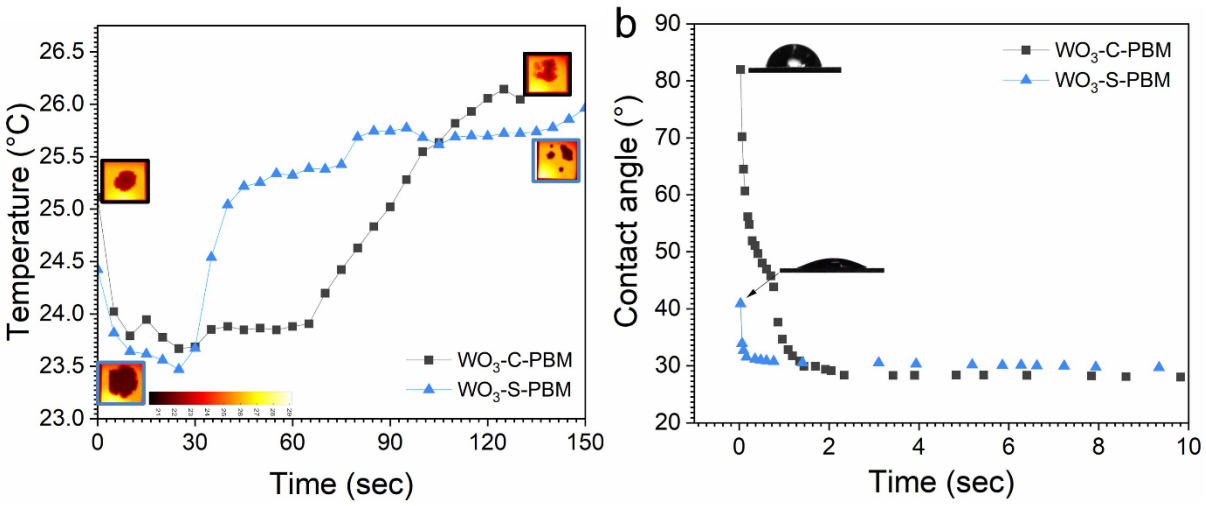

Figure 9. Contact angle and ink drying dynamics of WO_3-coated electrodes. (a) Temperature profiles assessed by infrared camera during ink droplet evaporation on Ni substrates heated to 50 °C, with thermal imaging snapshots showing initial (left) and final (right) drying stages for both samples. (b) Time-dependent contact angle evolution for KOH droplets on WO_3-C-BM and WO_3-SC-BM electrodes, with initial droplet snapshots at 0 s (insets) showing distinct wetting behavior. Scale bars represent temperature in °C.

Thermal imaging during evaporation confirms these interpretations. WO_3-C-PBM droplets exhibit pronounced "coffee ring" effects, with preferential particle accumulation at droplet edges creating non-uniform temperature distributions and concentrated deposition patterns. WO_3-S-PBM shows a substantially more uniform temperature distribution during drying, though some spatial heterogeneity remains, indicating reduced but not eliminated coffee ring behavior. These drying patterns arise from particle mobility differences: well-dispersed WO_3-S-PBM nanoparticles resist convective flow to edges, whereas partially aggregated WO_3-C-PBM particles readily concentrate at contact lines during evaporation [11].

Both WO_3-C-PBM and WO_3-S-PBM electrodes exhibit dynamic wetting with KOH, but with distinctly different initial surface characteristics (Figure 9 a). WO_3-C-PBM displays an initial contact angle of 82°, indicating hydrophobic surface character. The droplet rapidly spreads within the first 2 seconds, reaching an equilibrium of ~30° after approximately 5 seconds, where

it stabilizes. This abrupt wetting transition suggests capillary-driven absorption into the porous, cracked electrode structure revealed by SEM, rather than intrinsic surface hydrophilicity.

In contrast, WO_3-S-PBM exhibits an initial contact angle of 40°, demonstrating inherent hydrophilicity from the outset. The contact angle decreases more gradually, stabilizing at ~30° within 2-3 seconds. While both samples ultimately achieve similar equilibrium wettability, the 2-fold lower initial contact angle of WO_3-S-PBM reflects fundamentally different surface chemistry. This correlates directly with FTIR observations of enhanced surface hydroxylation (intensified O-H stretching at 3200-3600 cm^{-1}), where hydroxyl-rich surfaces promote immediate electrolyte affinity [47, 48]. The continuous, homogeneous coating morphology (SEM/AFM) combined with hydroxylated nanostructured surfaces enables an instant hydrophilic response, ensuring immediate and uniform electrolyte infiltration upon immersion in alkaline media. Conversely, the initially hydrophobic WO_3-C-BM (≈ 82°) reflects lower intrinsic hydroxylation, with rapid subsequent wetting driven by capillary infiltration into morphological defects rather than favorable surface energetics [11, 49].

These combined wettability and drying measurements provide a direct mechanistic link between powder properties, ink formulation and electrode morphology. The uniform, rapid drying of WO_3-S-PBM enabled by superior δD values (refer to Section 3.2) and hydroxylated surfaces promotes homogeneous deposition, yielding the continuous, crack-free coatings observed by SEM and AFM. Conversely, the slow, heterogeneous evaporation of WO_3-C-PBM with pronounced coffee ring formation produces the aggregated, voided morphology observed in SEM and AFM analysis. These distinct wetting and drying kinetics arise directly from intrinsic differences in precursor crystal quality: WO_3-S-PBM, consisting of uniformly sized nanoparticles, yields continuous electrode coatings, whereas WO_3-C-PBM, with heterogeneous particle size distributions, produces discontinuous films. This establishes precursor crystallinity as a critical material property governing electrode architecture and, as demonstrated in subsequent electrochemical characterization, catalytic performance[1].

3.4. Electrocatalytic Performance Evaluation

The electrochemical performance of the WO_3 samples was evaluated in 1 M KOH using a standard three-electrode setup, described in the experimental section. All studies were carried out by preparing electrodes from WO_3-C-PBM and WO_3-S-PBM inks drop-casted onto Ni rods. Prior to the OER measurements, the samples first underwent 50 cyclic voltammograms (CVs)

at 100 mV s^{-1} in a potential range of 0.4-1.6 V vs. RHE as a conditioning step to minimize contributions from transient surface species and establish electrochemical steady states.

Figure **10a** shows the conditioning CVs (1st and 50th cycle) of all samples. Both bare Ni and WO_3-C-PBM exhibit a redox peak of Ni^{2+}/Ni^{3+} at around 1.35 V vs. RHE corresponding to the β-$Ni(OH)_2$ → β-NiOOH transition [50]. In striking contrast, WO_3-S-PBM suppresses this β-phase signature while prominently activating γ-NiOOH formation at ~1.43 V vs. RHE [51, 52]. This peak is also present in the WO_3-C-PBM sample. However, its intensity is significantly lower than that observed for WO_3-S-PBM. This difference indicates that WO_3-S-PBM enables more effective phase-selective formation of the nickel oxyhydroxide species at the WO_3/Ni interface. Such behavior can be attributed to the more uniform and continuous surface morphology of WO_3-S-PBM, which exhibits enhanced surface roughness (see section 3.3.1) and a higher degree of surface hydroxylation (FTIR). The γ-phase, characterized by its disordered turbostratic structure, expanded interlayer spacing, and accessible high-valent Ni^{3+}/Ni^{4+} redox centers, is recognized as the intrinsically more active OER electrocatalyst compared to the ordered crystalline β-NiOOH[53]. All samples acquired a steady state over 50 conditioning cycles[54].

Figure **10b** depicts the LSVs of all investigated samples, acquired within the potential window of 1.3-1.8 V vs. RHE at a scan rate of 5 mV s^{-1}. The electrocatalytic performance was quantitatively assessed by comparing the geometric current densities extracted at a fixed potential of 1.65 V vs. RHE. As evident from the LSV profiles, WO_3-S-PBM exhibits markedly enhanced OER performance, delivering a current density of 84.76 mA cm^{-2}, which is nearly 3-fold higher than that of WO_3-C-PBM (~28 mA cm^{-2}). This superior activity is further corroborated by the significantly reduced overpotential required to reach 10 mA cm^{-2} on WO_3-S-PBM (328 mV), relative to both bare Ni (348 mV) and WO_3-C-PBM (375 mV). The comparative evaluation of these electrocatalysts, summarized in Figure **10c**, clearly highlights the pronounced performance advantage of the single-crystal-derived architecture, underscoring its enhanced intrinsic activity and more favorable reaction kinetics. This correlates directly with the γ-NiOOH-dominated interface established during preconditioning; the nanostructured WO_3-S-PBM selectively stabilizes the intrinsically more active disordered γ-phase, whereas WO_3-C-PBM favors the less active crystalline β-NiOOH [52].

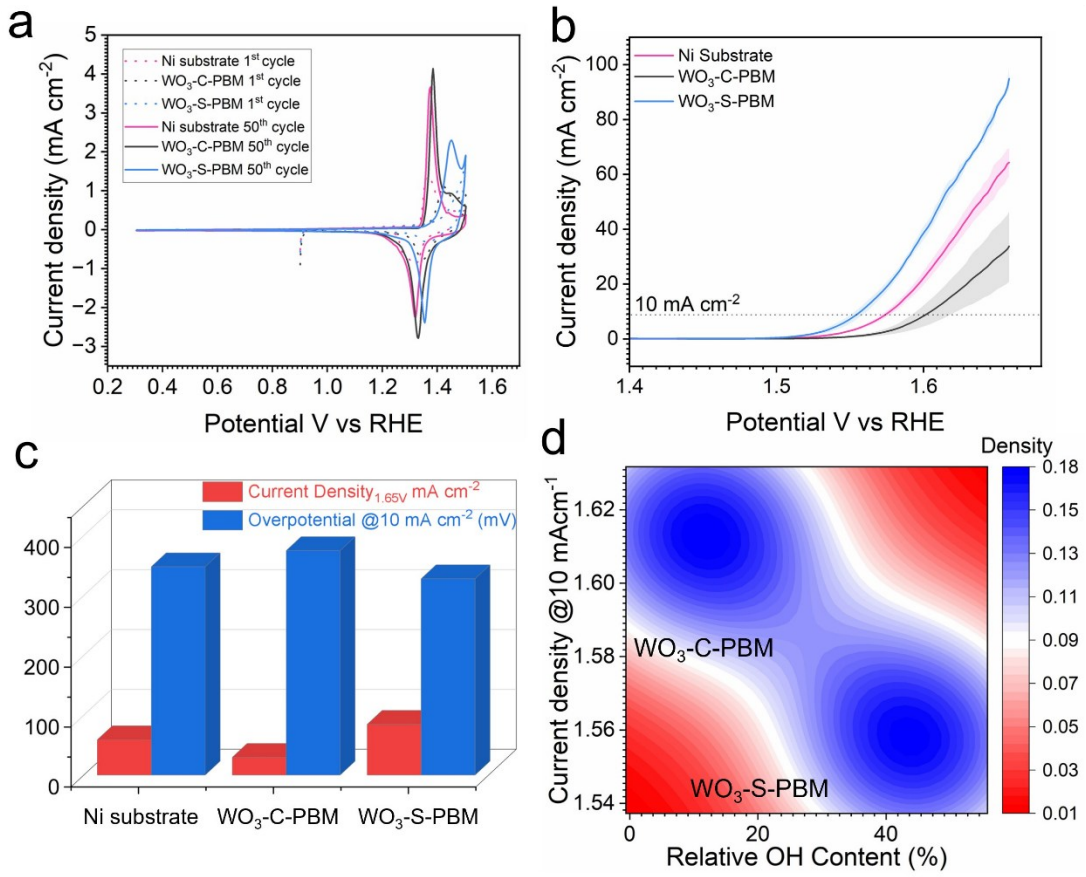

Figure 10. Electrochemical characterization of the WO_3 ball milled and Ni rod for a comparative study. (a, b) CVs and LSVs of the samples and (c) comparisons of current density measured at 1.65 V vs. RHE, overpotential measured at 10 mA cm^{-2}. d) contour plot correlating relative surface hydroxylation (FTIR-derived O-H content, x-axis) with overpotential at 10 mA cm^{-2} (y-axis), demonstrating the inverse relationship between surface hydroxyl groups and OER kinetic barrier. All electrochemical measurements performed in 1 M KOH.

To further explore the underlying electrochemical behavior, the ECSA was determined from EIS measurements at open circuit potential in the non-Faradaic region (**Figure S6**). Based on this analysis, WO_3-C-PBM exhibits an effective double-layer capacitance of 3.75×10^{-6} F, while WO_3-S-PBM shows a marginally higher value of 3.94×10^{-6} F. The corresponding electrochemically active surface areas (ECSAs) show higher value for WO_3-S-PBM (0.0985 cm^2) compared to that of WO_3-C-PBM (0.0938 cm^2). To further elucidate the origin of this activity enhancement, the relationship between surface chemistry and electrochemical performance was examined (Figure 10d). A contour plot correlating relative surface hydroxylation (quantified from FTIR OH stretching intensities) with overpotential at 10 mA cm^{-2} reveals a strong inverse correlation: WO_3-S-PBM, exhibiting the highest OH content, achieves the lowest overpotential (328 mV), while WO_3-C-PBM with lower hydroxylation requires significantly higher overpotential (375 mV). This demonstrates that enhanced surface

hydroxylation enabling facile OH^- adsorption and rapid proton-coupled electron transfer directly reduces the kinetic barrier for OER[55].

Combined with the preconditioning CV evidence (Figure 10a) showing phase-selective γ-NiOOH stabilization at the WO_3-S-PBM/Ni interface, these results establish a clear structure–activity relationship: the nanostructured single-crystal-derived morphology with enhanced surface hydroxylation uniquely favors formation of the disordered, high-valent Ni^{4+}-rich γ-NiOOH phase over crystalline β-NiOOH. Thus, performance gains arise from synergistic effects of interfacial phase selectivity and optimized surface chemistry rather than geometric surface area expansion.

The integrated structure activity analysis reveals that this electrochemical superiority emerges from synergistic characteristics of WO_3-S-PBM:

- Optimized film morphology and interfacial contact (SEM/AFM): Ball milling of the single-crystal precursor produces uniform ~20-50 nm nanoparticles that form better coatings with enhanced nanoscale roughness and homogeneity, creating dense, intimate WO_3/Ni interfacial contact across the entire electrode facilitating uniform γ-NiOOH formation. This contrasts with the morphology of WO_3-C-PBM.
- Enhanced surface hydroxylation and favorable wetting (FTIR/contact angle): Intensified O-H stretching bands (3200-3600 cm^{-1}) correlate with 2-fold lower initial contact angle ($\theta_0 \approx 40°$ vs. 82°), facilitating immediate electrolyte infiltration and rapid OH^- adsorption kinetics, the rate-determining step in alkaline OER. While both samples achieve similar equilibrium wetting (~30° after 2 s), the inherent hydrophilicity of WO_3-S-PBM ensures immediate uniform electrolyte distribution upon immersion.
- Uniform ink drying and homogeneous deposition (evaporation dynamics): Rapid, spatially uniform evaporation (temperature minimum at 20 s vs. 40 s for C-PBM) with minimal coffee ring formation enables homogeneous particle deposition, directly producing the continuous coating morphology. Conversely, slow, heterogeneous drying of WO_3-C-PBM promotes edge-concentrated particle accumulation and voided regions.

4. Conclusions

In conclusion, we have demonstrated how the interplay of intrinsic precursor properties (crystallinity and phase composition: WO_3-C versus WO_3-S) and extrinsic mechanochemical activation affects alkaline OER catalytic performance through deterministic control over

electrode morphology and interfacial phase selectivity. This study presents for the first time a systematic framework to disentangle these intrinsic material characteristics from extrinsic processing-induced modifications, establishing their interplay as a critical, previously overlooked design parameter governing interfacial phase selectivity and OER activity in metal-oxide composite electrocatalysts. Optimizing catalyst performance thus requires understanding how starting material architecture propagates through processing to determine interfacial electrochemistry.

Both WO_3-C and WO_3-S, initially present as large (~400 nm) faceted particles, were subjected to identical planetary ball milling protocols to yield nanocrystalline powders. Despite achieving comparable particle size reduction, the two precursors yield fundamentally different materials: WO_3-S-PBM produces uniform 20–30 nm particles with enriched γ-monoclinic phase content (40% vs. 28%), superior dispersion stability, and continuous electrode coatings, whereas WO_3-C-PBM yields heterogeneous aggregates with voided, cracked morphology.

On the powder level, synchrotron pair distribution function analysis confirmed preserved local WO_6 octahedral geometry with precursor-dependent medium-range structural homogenization. FTIR spectroscopy demonstrated enhanced surface hydroxylation for WO_3-S-PBM (intensified O-H bands at 3200-3600 cm^{-1}), correlating with 2-fold lower initial contact angle and more favorable wetting kinetics. Time-dependent thermal imaging revealed distinct ink drying behavior: WO_3-C-PBM exhibits slow, heterogeneous evaporation with coffee ring formation promoting edge-concentrated particle accumulation, whereas WO_3-S-PBM shows uniform, rapid drying that suppresses such effects. Combined SEM and AFM analysis established that these drying kinetics translate to end-state morphology WO_3-C-PBM produces discontinuous films, while WO_3-S-PBM yields continuous, crack-free coatings with controlled nanoscale roughness (5-fold lower variability), enabling dense WO_3/Ni interfacial contact.

These synergistic structural and processing advantages manifest in substantial OER performance enhancement: WO_3-S-PBM/Ni delivers 84.76 mA cm^{-2} at 1.65 V vs. RHE with an overpotential of 328 Mv representing 3-fold current density enhancement and 47 mV overpotential reduction compared to WO_3-C-PBM (η = 375 mV). Electrochemical impedance spectroscopy revealed nearly identical active surface areas (<3% difference), unambiguously establishing that the performance gain reflects enhanced intrinsic turnover frequency rather than geometric surface area effects. Mechanistically, cyclic voltammetry during electrochemical conditioning demonstrated that WO_3-S-PBM selectively stabilizes the intrinsically more active γ-NiOOH phase (1.45 V vs. RHE) with its disordered structure and accessible Ni^{3+}/Ni^{4+} redox

centers, whereas WO_3-C-PBM's non-uniform coating permits mixed β/γ phase coexistence with incomplete phase control. This establishes that WO_3 is not an OER active site per se but can be activated by tailoring the interplay of precursor crystallinity and mechanochemical processing, as it is this interplay that governs which nickel oxyhydroxide phase forms at the WO_3/Ni interface the true determinant of catalytic activity.

The systematic workflow employed here comparing precursors of identical composition but different crystal quality through mechanochemical nanostructuring, ink formulation, and multi-scale characterization provides a generalizable blueprint for evaluating how starting material architecture propagates through processing to determine electrocatalytic performance. Precursor crystallinity determines particle fragmentation pathways, surface chemistry, dispersion stability, drying uniformity, and ultimately electrode-scale interfacial homogeneity, enabling 3-fold activity enhancement through this single parameter. These results demonstrate that earth-abundant oxides like WO_3, often dismissed due to processing challenges, can achieve competitive OER performance when feed material-to-electrode transformation is systematically controlled. Critically, interfacial phase selectivity rather than intrinsic oxide activity governs performance, establishing new design principles centered on tailoring metal-oxide interfaces for desired nickel hydroxide/oxyhydroxide phase stabilization. This precursor-centric approach, combined with mechanochemical activation, could be extended to other oxide/metal combinations, offering a general strategy for high-performing, scalable, earth-abundant electrocatalysts in next-generation alkaline water electrolyzers.

Acknowledgement

The authors acknowledge the financial support from the Federal Ministry of Research, Technology and Space (BMFTR project “PrometH2eus”, FKZ 03HY105F). We are also grateful for the support provided by the Mercator Research Center Ruhr (MERCUR.Exzellenz, ‘DIMENSION’ Ex-2021-0034). This work was also funded by the UDE Postdoc Seed Funding. DS acknowledge the Mat4Hy consortium for cooperative support. Parts of this project have received funding from the European Research Council (ERC) under the European Union’s Horizon 2020 research and innovation program (grant agreement No. 863823 MATTER), which is gratefully acknowledged by G.S. Open Access funding was facilitated and organized by Projekt DEAL. M.S. and O.K. acknowledge funding by the DFG via IRTG 2803 “2D Mature”, project number 461605777 and via project number 429784087. We extend our thanks to Dr. Markus Heidelmann from the Interdisciplinary Center for Analytics on the Nanoscale

(ICAN) for their valuable assistance. Blaž Toplak for the XPS measurements and Jacob Johny for SEM analysis.

Supporting Information

Supplementary data to this article can be found online at XXX

Data availability

The data that support the findings of this study are openly available in Zenodo at XXX

Declaration of generative AI and AI-assisted technologies in the writing process

During the preparation of this work the authors used the AI Perplexity in order to improve the readability and language of the manuscript. After using this tool/service, the authors reviewed and edited the content as needed and take full responsibility for the content of the published article.

References

1. Vinayakumar, V., et al., *Ni-Co-O anodes for the alkaline oxygen evolution reaction: Multistage electrode optimization and plasma-assisted activity enhancement enabled by a coherent workflow.* Chemical Engineering Journal, 2025: p. 167169.
2. Tüysüz, H., *Alkaline water electrolysis for green hydrogen production.* Accounts of Chemical Research, 2024. **57**(4): p. 558-567.
3. Li, J., *Oxygen evolution reaction in energy conversion and storage: design strategies under and beyond the energy scaling relationship.* Nano-Micro Letters, 2022. **14**(1): p. 112.
4. Fabbri, E. and T.J. Schmidt, *Oxygen evolution reaction—the enigma in water electrolysis*. 2018, ACS Publications. p. 9765-9774.
5. Nocera, D.G., *Proton-coupled electron transfer: the engine of energy conversion and storage.* Journal of the American Chemical Society, 2022. **144**(3): p. 1069-1081.
6. Xie, X., et al., *Oxygen evolution reaction in alkaline environment: material challenges and solutions.* Advanced Functional Materials, 2022. **32**(21): p. 2110036.
7. Ehlers, J.C., et al., *Affordable green hydrogen from alkaline water electrolysis: key research needs from an industrial perspective.* ACS Energy Letters, 2023. **8**(3): p. 1502-1509.
8. Naito, T., et al., *Recent advances in understanding oxygen evolution reaction mechanisms over iridium oxide.* Inorganic Chemistry Frontiers, 2021. **8**(11): p. 2900-2917.
9. Daiane Ferreira da Silva, C., et al., *Oxygen evolution reaction activity and stability benchmarks for supported and unsupported IrO x electrocatalysts.* ACS Catalysis, 2021. **11**(7): p. 4107-4116.
10. Yu, M., E. Budiyanto, and H. Tüysüz, *Principles of water electrolysis and recent progress in cobalt-, nickel-, and iron-based oxides for the oxygen evolution reaction.* Angewandte chemie international edition, 2022. **61**(1): p. e202103824.
11. Jain, A., et al., *Wetting across the Lyophilic–Lyophobic Spectrum: Morphological Tuning of Anode Catalyst Layers for the Alkaline Oxygen Evolution Reaction.* ACS Applied Materials & Interfaces, 2025.
12. Ede, S.R. and Z. Luo, *Tuning the intrinsic catalytic activities of oxygen-evolution catalysts by doping: a comprehensive review.* Journal of Materials Chemistry A, 2021. **9**(36): p. 20131-20163.

13. Han, Y., et al., *Stability challenges and opportunities of NiFe-based electrocatalysts for oxygen evolution reaction in alkaline media.* Carbon Neutralization, 2024. **3**(2): p. 172-198.
14. Ciambriello, L., et al., *Unexpected resilience of NiFe catalysts for the alkaline oxygen evolution reaction.* ACS Applied Energy Materials, 2024. **7**(8): p. 3462-3472.
15. Boateng, E., et al., *Synthesis and electrochemical studies of WO3-based nanomaterials for environmental, energy and gas sensing applications.* Electrochemical Science Advances, 2022. **2**(5): p. e2100146.
16. Yao, Y., et al., *A review on the properties and applications of WO3 nanostructure-based optical and electronic devices.* Nanomaterials, 2021. **11**(8): p. 2136.
17. Mehboob, A., et al., *Enhanced OER performance by varying Al-WO3 electrocatalyst thickness: process optimization.* Results in Engineering, 2024. **22**: p. 102322.
18. Wang, Y., et al., *In-situ etching synthesis of 3D self-supported serrated Ni-WO3 for oxygen evolution reaction.* Journal of Alloys and Compounds, 2022. **893**: p. 162134.
19. Besnardiere, J., et al., *Structure and electrochromism of two-dimensional octahedral molecular sieve h'-WO3.* Nature Communications, 2019. **10**(1): p. 327.
20. Li, H., et al., *Oxygen vacancy-mediated WO3 phase junction to steering photogenerated charge separation for enhanced water splitting.* Journal of Advanced Ceramics, 2022. **11**(12): p. 1873-1888.
21. Linderalv, C., *Structural and thermodynamical properties of tungsten oxides from firstprinciples calculations*. 2016, Master's thesis, Chalmers University of Technology.
22. Ji, X., et al., *WO3 nanoarray: an efficient electrochemical oxygen evolution catalyst electrode operating in alkaline solution.* Inorganic Chemistry, 2017. **56**(24): p. 14743-14746.
23. Li, Y., et al., *Defect engineering of air-treated WO3 and its enhanced visible-light-driven photocatalytic and electrochemical performance.* The Journal of Physical Chemistry C, 2016. **120**(18): p. 9750-9763.
24. Ma, Q., et al., *Interfacial internal-electric field on nanoneedle CoOOH/WO3 photoelectrode realized efficient photoelectrocatalytic degradation of 4-fluorophenol via facilitated H2O oxidation and physical contact.* Chemical Engineering Journal, 2024. **498**: p. 155551.
25. Knöppel, J., et al., *Photocorrosion of WO3 photoanodes in different electrolytes.* ACS physical chemistry Au, 2021. **1**(1): p. 6-13.
26. Jafari, F., et al., *A new OER electrocatalyst based on WO3 decorated with Ni2CoS4.* Inorganic Chemistry Communications, 2025. **173**: p. 113849.
27. Li, Y., et al., *WO3-based materials as electrocatalysts for hydrogen evolution reaction.* Frontiers in Materials, 2020. **7**: p. 105.
28. Kunzmann, A., et al., *Synthesis and characterization of WO3 single crystals by physical vapor transport method.* Journal of Crystal Growth, 2025: p. 128475.
29. Chatwani, M., et al., *Mechanochemical activation of nickel oxide: a pivotal step in the process chain enabling binder-free-anodes for alkaline water electrolysis.*
30. Bhandari, S., et al., *Exploring the Effect of Ball Milling on the Physicochemical Properties and Oxygen Evolution Reaction Activity of Nickel and Cobalt Oxides.* Advanced Energy and Sustainability Research, 2024. **5**(12): p. 2400183.
31. Diehl, R., G. Brandt, and E. Salje, *The crystal structure of triclinic WO3.* Structural Science, 1978. **34**(4): p. 1105-1111.
32. Salje, E., *Lattice dynamics of WO3.* Foundations of Crystallography, 1975. **31**(3): p. 360-363.
33. Daniel, M., et al., *Infrared and Raman study of WO3 tungsten trioxides and WO3, xH2O tungsten trioxide tydrates.* Journal of solid state chemistry, 1987. **67**(2): p. 235-247.
34. Song, W., et al., *Exposed crystal facets of WO3 nanosheets by phase control on NO2-sensing performance.* Journal of Materials Science: Materials in Electronics, 2020. **31**(1): p. 610-620.
35. Kuzmin, A., et al., *X-ray diffraction, extended x-ray absorption fine structure and Raman spectroscopy studies of WO 3 powders and (1− x) WO 3− y· x ReO 2 mixtures.* Journal of applied Physics, 1998. **84**(10): p. 5515-5524.
36. Gotić, M., et al., *Synthesis of tungsten trioxide hydrates and their structural properties.* Materials Science and Engineering: B, 2000. **77**(2): p. 193-201.
37. Shigesato, Y., et al., *Characterization of evaporated amorphous WO3 films by Raman and FTIR spectroscopies.* Applied Surface Science, 1988. **33-34**: p. 804-811.

38. Kanan, S.M., et al., *Identification of surface sites on monoclinic WO3 powders by infrared spectroscopy.* Langmuir, 2002. **18**(5): p. 1707-1712.
39. Ng, L.Y.F., et al., *High-energy ball milling for high productivity of nanobiochar from oil palm biomass.* Nanomaterials, 2022. **12**(18): p. 3251.
40. Nayak, S.S., et al., *Selective colloidal synthesis of hexagonal and monoclinic substoichiometric tungsten oxide nanocrystals as dual-band electrochromic materials.* Chemistry of Materials, 2025. **37**(21): p. 8764-8774.
41. Solonin, Y.M., O.Y. Khyzhun, and E. Graivoronskaya, *Nonstoichiometric tungsten oxide based on hexagonal WO3.* Crystal Growth & Design, 2001. **1**(6): p. 473-477.
42. Anwar, O., et al., *Hansen parameter evaluation for the characterization of titania photocatalysts using particle size distributions and combinatorics.* Nanoscale, 2022. **14**(37): p. 13593-13607.
43. Bapat, S., et al., *Towards a framework for evaluating and reporting Hansen solubility parameters: applications to particle dispersions.* Nanoscale Advances, 2021. **3**(15): p. 4400-4410.
44. Amin, A.S., et al., *A Procedure for Rational Probe Liquids Selection to Determine Hansen Solubility Parameters.* ChemCatChem, 2024. **16**(6): p. e202301393.
45. Süß, S., et al., *Determination of Hansen parameters for particles: A standardized routine based on analytical centrifugation.* Advanced Powder Technology, 2018. **29**(7): p. 1550-1561.
46. Hansen, C.M., *Hansen solubility parameters: a user's handbook*. 2007: CRC press.
47. Jothiramalingam, R., et al., *Synthesis and physico-chemical characterization of WO3-TiO2 type composite materials for efficient electrochromic applications.*
48. Turan, E. and T. Caykara, *Construction of hydroxyl-terminated poly (N-isopropylacrylamide) brushes on silicon wafer via surface-initiated atom transfer radical polymerization.* Journal of Polymer Science Part A: Polymer Chemistry, 2010. **48**(17): p. 3880-3887.
49. Vinayakumar, V., et al., *A Proof of Principle for the Phase-Dependent Electrocatalytic Activity of NiTi Shape Memory Alloys for Oxygen Evolution Reaction.*
50. Zhang, P., et al., *Dendritic core-shell nickel-iron-copper metal/metal oxide electrode for efficient electrocatalytic water oxidation.* Nature communications, 2018. **9**(1): p. 381.
51. Fernández, H.M., et al., *Phase transitions in NiO during the oxygen evolution reaction assessed via electrochromic phenomena through operando UV–Vis spectroscopy.* Electrochimica Acta, 2024. **498**: p. 144626.
52. Bhosale, N. and A. Kadam, *Superior electrochromic performance of tungsten oxide embedded with polypyrrole.* Int. J. Innov. Res. Sci. Technol., 2016. **3**: p. 106-110.
53. Wang, B., et al., *Enhancing the oxygen evolution reaction by tuning the electrode–electrolyte interface in nickel-based electrocatalysts.* Communications Chemistry, 2025. **8**(1): p. 109.
54. Trafela, Š., et al., *Controllable voltammetric formation of a structurally disordered NiOOH/Ni (OH) 2 redox pair on Ni-nanowire electrodes for enhanced electrocatalytic formaldehyde oxidation.* Electrochimica Acta, 2020. **362**: p. 137180.
55. Yang, C., et al., *Surface hydroxylation engineering to boost oxygen evolution reaction on IrO2/TiO2 for PEM water electrolyzer.* Applied Catalysis B: Environment and Energy, 2024. **358**: p. 124462.

Supporting Information

Intrinsic Alkaline OER Activity in Mechanochemically Activated WO_3 from Commercial and Single-Crystal Precursors

Vineetha Vinayakumar[1,2], Mohit Chatwani[1], Aneeta Jose[1], Osamah Kharsah[2,3], Hao Yun[1], Adithya Aravind[1], Adarsh Jain[1], Ahmed Suhail Odungatu[1], Alexander Kunzmann[4,5], Gabi Schierning[2,4,5], Sabrina Disch[2,6], Marika Schleberger[2,3], Doris Segets[1,2*]*

1. Supplementary Figures, Tables and discussions

1.1 Structural, Microstructural, and Chemical Characterization

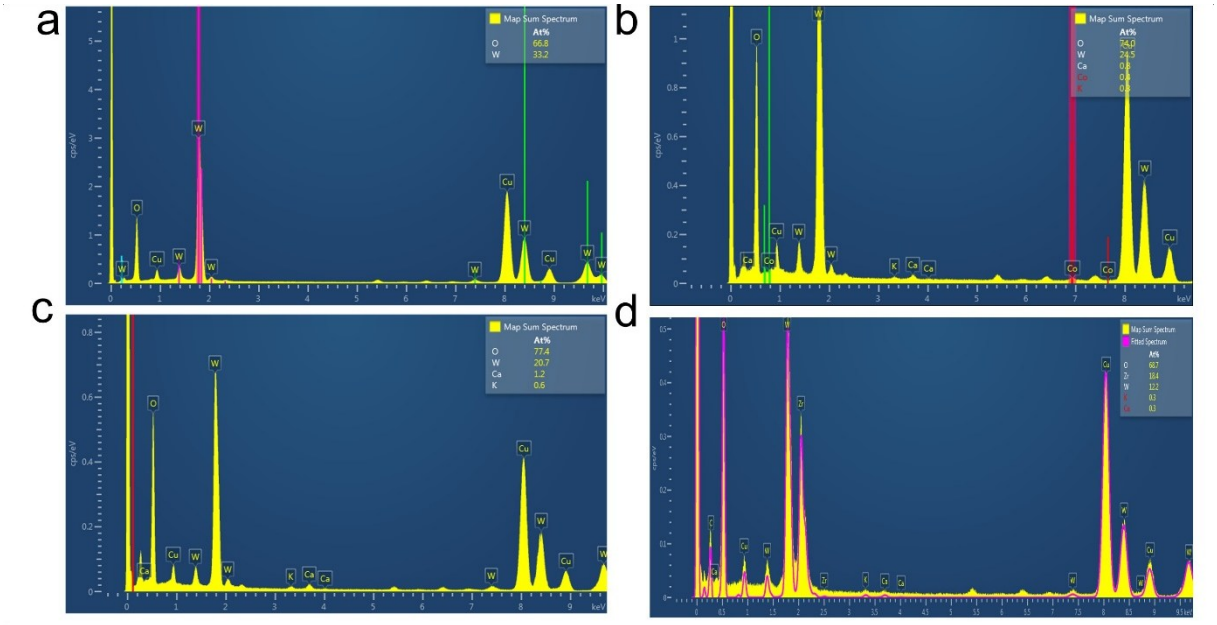

***Figure S1**. Energy-Dispersive X-ray Spectroscopy (EDX) analysis of WO_3 precursors and Planetary ball-milled (PBM) powders. (a,b) Pre-milling WO_3-C/S: faceted particles, pure W/O spectra. (c,d) Post-milling WO_3-C-PBM/S-PBM: nanocrystallites showing O-enriched surfaces (77/20 at% O/W), trace Ca/K/Zr. Elemental maps confirm homogeneous W/O distribution across particles*

Table ST1 Relative OH Content of WO_3 feed and PBM samples

Material	Relative OH Content (%)
WO_3-C	10.9
WO_3-C-PBM	11.1
WO_3-S	~0
WO_3-S-PBM	44.3

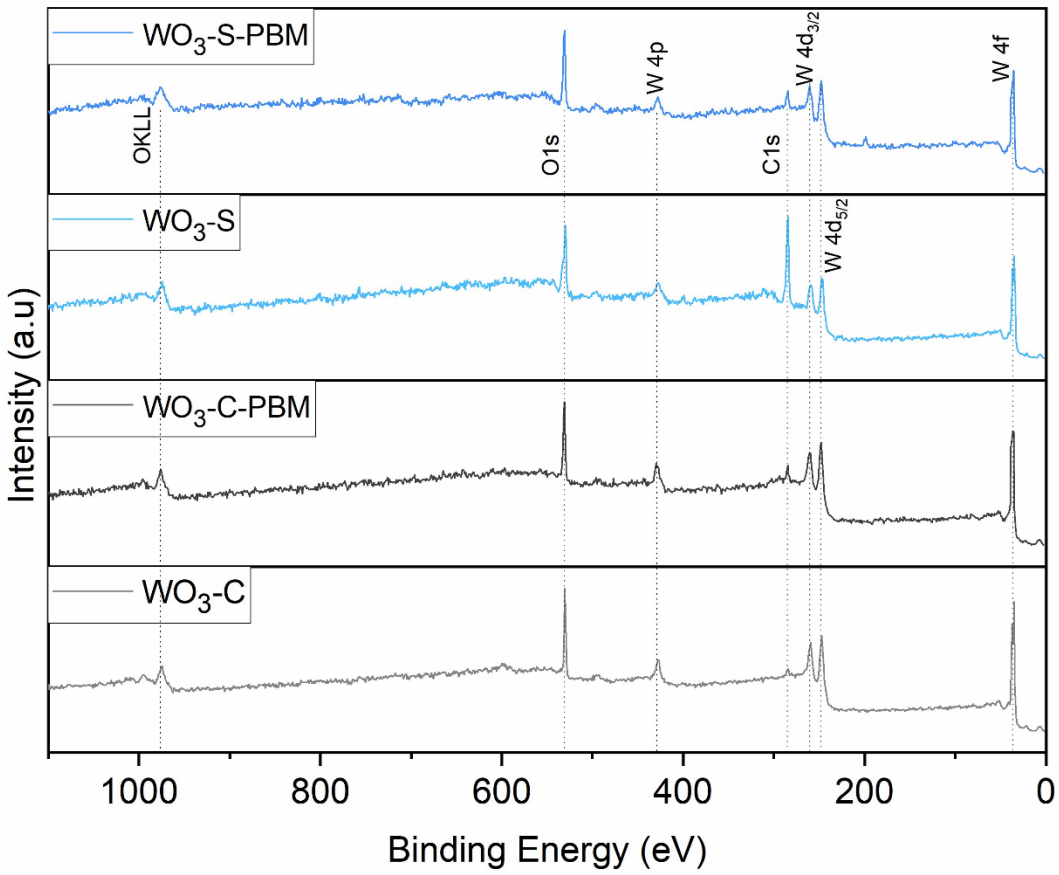

Figure S2. *XPS survey spectra of WO_3-C, WO_3-C-PBM, WO_3-S, and WO_3-S-PBM, with significant elemental peaks marked.*

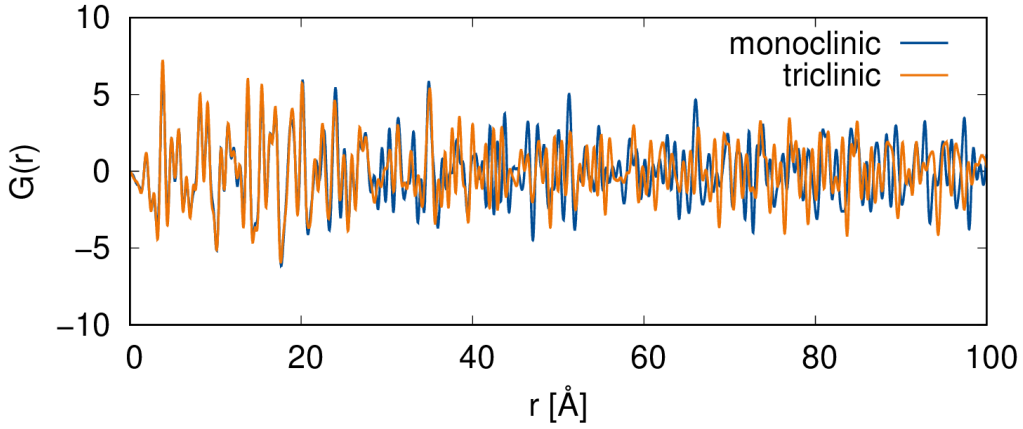

Figure S3. *Calculated PDF for monoclinic γ-WO_3 and triclinic δ-WO_3*

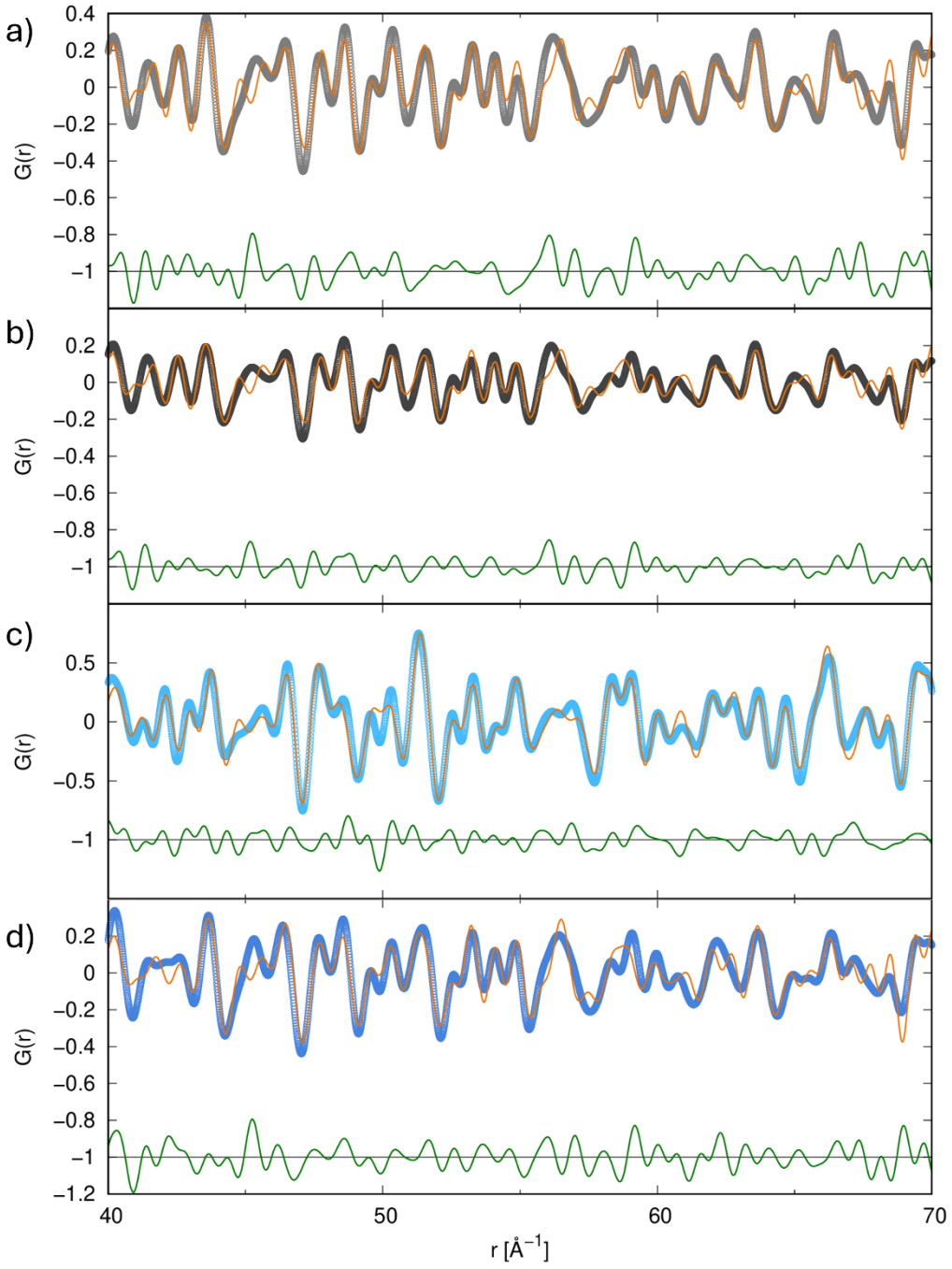

Figure S4. *PDF fits in a range of 40 Å < r < 70 Å for a) WO_3-C, b) WO_3-C-PBM, c) WO_3-S, and d) WO_3-S-PBM (orange: fit; green: difference)*

Table ST2. PDF fit results for the monoclinic γ-WO_3 and triclinic δ-WO_3 phases (Fig. S4). Lattice parameters (a,b,c) are given in Å, angular parameters (α,β,γ) are given in °.

		WO_3-C	WO_3-S	WO_3-C-PBM	WO_3-S-PBM
δ-WO_3,	a	7.36	7.30	7.36	7.36
	b	7.51	7.52	7.50	7.50
	c	7.69	7.69	7.69	7.69
	α	88.9	88.9	88.9	89.0
	β	90.9	90.9	90.9	90.8
	γ	90.9	90.9	91.0	91.0
γ-WO_3,	a	7.31	7.31	7.31	7.31
	b	7.56	7.54	7.56	7.54
	c	7.68	7.71	7.68	7.69
	β	90.9	90.8	90.8	90.9
δ-WO_3 : γ-WO_3		73(6):27(6)	48(5):52(5)	72(10):28(10)	60(7):40(7)

1.2. WO_3 ink formulation

The sedimentation behavior of the finally prepared inks is shown in **Figure S5**. Transmittograms [1, 2] were applied to analyze dispersions prepared in water-IPA mixture with Sustainion binder. In brief, these contour plots can be generated from centrifugation data and illustrate time and space-resolved transmission. They offer insights into sedimentation dynamics and colloidal stability.

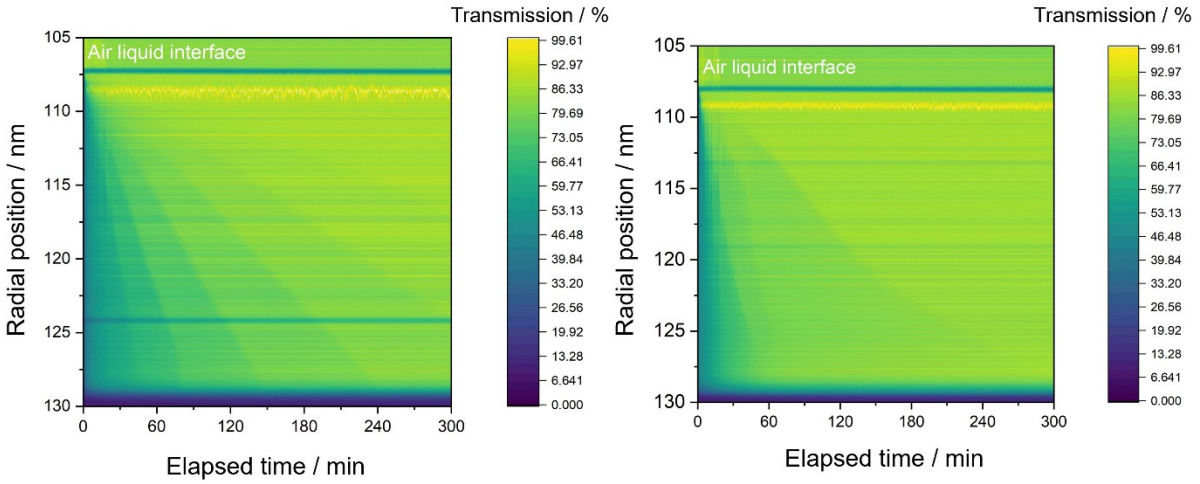

***Figure S5**: Visualization of the time-resolved sedimentation process via transmittograms: Ink prepared based on (a) WO_3-C-PBM, and (b) WO_3-S-PBM, using a mixture of water and IPA as continuous phase (1:1 volume ratio) and Sustainion as a binder.*

In each transmittogram, the x-axis represents the elapsed time since centrifugation began, and the y-axis shows the radial position within the centrifuge cell. Transmission values are represented by varying yellow tones, with darker tones indicating higher levels of light blockage

due to scattering, corresponding to higher particle concentration at a given time and position. All measurements were performed at 2500 rpm, corresponding to the centrifugal acceleration of approximately 550 g, indicating that both WO_3-C-PBM and WO_3-S-PBM-based inks exhibit sufficient sedimentation stability to form reliable coatings under standard gravity. However, transmittogram analysis revealed notable differences in the sedimentation behavior between the two formulations where the only difference was the chosen active material. WO_3-C-PBM-based inks demonstrated significantly higher stability, with the majority of particles settling over a period of ~80 minutes, while smaller particles remained suspended beyond 120 minutes. In contrast, WO_3-S-PBM inks displayed relatively faster sedimentation, with most particles settling within ~60 minutes. Extrapolating to normal gravitational conditions, complete sedimentation would take approximately 30 days for WO_3-C-PBM and around 23 days for WO_3-S-PBM, assuming no particle agglomeration occurs.

Table ST3. Parameters utilized in MSDQ: Homogeneity score (Hs) at different region of selection (ROS), standard deviation (σ), margin of error (E), confidence interval (α) and optimal number of ROS (x) for WO_3-C-PBM and WO_3-S-PBM.

Parameters	WO_3-C-PBM	WO_3-S-PBM
$H_{s\,(ROS1)}$ /-	0.97312	0.976
$H_{s\,(ROS2)}$ /-	0.90634	0.93537
$H_{s\,(ROS3)}$ /-	0.94564	0.86147
$H_{s\,(ROS4)}$ /-	0.81249	0.69776
σ /-	0.0702	0.1228
E /%	10%	10%
α /%	90%	90%
x_z /-	4	4
x /-	0.97312	0.976

1.3 Electrochemical Impedance Spectroscopy

The impedance spectra were fitted to a simplified two-element circuit model $R_u + Q_1$, where Q_1 represents the double-layer constant phase element (CPE) and R_u is the uncompensated solution resistance. CPE formalism accounts for non-ideal capacitive behavior arising from surface heterogeneity and roughness. The coefficient α ($0 < \alpha \leq 1$) quantifies how far the capacitive behavior deviates from the ideal behavior, with $\alpha = 1$ representing an ideal capacitor. EIS fitting for each sample is shown in Figure S3. The Q_1 value can be correlated with effective capacitance (C_{eff}), and the formula for the effective capacitance as a function of constant phase element (CPE) is given in the general form as $C_{eff} = Q_1^{\frac{1}{a}} \left(\frac{1}{R_u} + \frac{1}{R_{ct}}\right)^{\frac{a-1}{a}}$. However, since the EIS was measured at OCP, where no Faradaic reaction takes place, $R_{ct} \rightarrow \infty$, simplifying the expression to Equation 1[3-5]:

$$C_{eff} = Q_1^{\frac{1}{a}} R_1^{\frac{a-1}{a}} \quad (1)$$

where Q_1 is the double-layer CPE and R_u is the solution resistance.

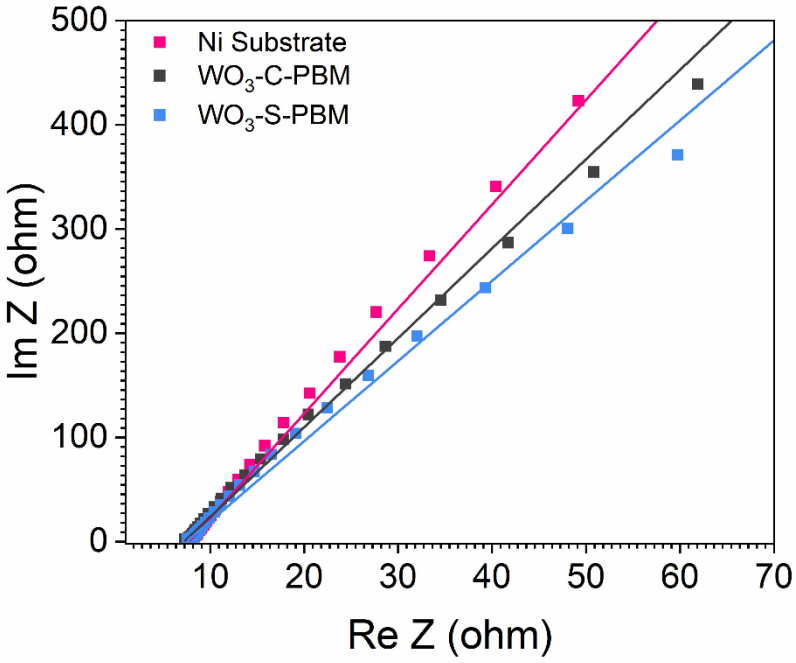

Figure S6. Electrochemical Impedance Spectroscopy (EIS) Comparison of WO_3-C-PBM and WO_3-S-PBM on Ni Rod Electrodes in 1 M KOH.

2. Materials and Characterization methods

2.1 Materials

Ethanol (EtOH), Dimethylformamide (DMF), and Tetrahydrofuran (THF), Isopropanol (IPA), dimethyl sulfoxide (DMSO), N-Methyl-2-pyrrolidone (NMP), and polycarbonate (PC)

2.2 TEM- EDX

The morphology and elemental distribution of all four powders, WO_3-C, WO_3-S, WO_3-C-PBM and WO_3-S-PBM powders were determined using TEM with in-built EDX. TEM-EDX measurements were conducted using a JEOL JEM-2200FS microscope, and the sample was obtained by drying an aliquot of the micron-sized powder upon dispersion in an organic solvent by ethanol and drop-casting on a carbon-coated Cu grid under ambient conditions.

2.2 X-Ray diffraction

Synchrotron X-ray total scattering measurements were performed at beamline ID31 at the European Synchrotron Radiation Facility (ESRF). As for TEM sample preparation, WO_3-S crystal with nominal stoichiometric composition was gently ground using an agate mortar to obtain a fine powder suitable for X-ray diffraction analysis. The sample powders were loaded into cylindrical slots (approx. 1 mm thickness) held between Kapton windows in a high-throughput sample holder. Each sample was measured in transmission geometry with an incident X-ray energy of 75.051 keV (λ = 0.16520 Å). Measured intensities were collected using a Pilatus CdTe 2M detector (1679 × 1475 pixels, 172 × 172 μm2 each) positioned with the incident beam in the corner of the detector. The sample-to-detector distance was approximately 1.5 m. Data was processed into the PDF with a Qmax = 8.7Å-1 using the xPDFsuite[6]. The PDF data was evaluated using the PDFgui program [7].

2.3 Raman Spectroscopy

To investigate the vibrational modes' characteristic and confirm the phase composition of WO_3, Raman spectroscopy measurements were performed. All powder samples were carefully put onto a glass slide and were analyzed at room temperature using a WITec alpha300 RA confocal Raman spectrometer with 532 nm laser wavelength, a power output of 1 mW, and a spot diameter < 2 μm (20x objective lens). Signal integration time was 10 s. The measurement was performed using a grid with 600 g/mm.

2.4 Fourier Transform Infrared Spectroscopy (FTIR)

Fourier Transform Infrared spectroscopy was conducted to investigate the functional groups and chemical bonding in the anode materials using a FTIR spectrometer (Bruker, Vertex 80). The instrument was equipped with a RT-DLaTGS (Room Temperature Deuterated L-Alanine doped TriGlycine Sulphate) detector and a KBr beam splitter. The transmittance spectra were recorded in attenuated total reflectance (ATR) mode over the range of 4000–400 cm-1with a spectral resolution of 4 cm-1. The measurements were conducted at RT under N2 atmosphere to prevent moisture and CO_2 interference. Each spectrum was obtained by averaging 32 scans on three different spots for each sample to improve the signal-to-noise ratio and reproducibility. The obtained spectra were then subjected to baseline correction and normalization using Bruker OPUS9.0 software to enhance the clarity and accuracy of the peaks.

2.5 X-ray Photoelectron Spectroscopy (XPS)

Surface compositions of WO_3-C, WO_3-S, WO_3-C-PBM and WO_3-S-PBM specimens were determined by X-ray photoelectron spectroscopy (XPS). XPS measurements were conducted employing a ULVAC-PHI Versaprobe II device (Chanhassen, USA). The samples were analyzed applying an Al Kα radiation (hν = 1253.6eV) with a band-pass energy of 11.75 eV. As a reference, the XPS spectra were calibrated using the C1s adventitious carbon C–C binding energy at 284.8 eV. All spectra were analyzed with the CasaXPS 2.3.25 software.

2.6 X-ray photoelectron spectroscopy

Surface compositions of the Ni-Co-O films as well as the micropowder feed were determined employing XPS. XPS measurements were conducted employing a custom-designed near ambient pressure (NAP) XPS under ultra-high vacuum (~10^{-8} mbar). The system was equipped with an Al-Kα X-ray source with monochromated X-rays having an energy of 1486.6 eV. The peak deconvolution as well as data analysis was performed using CasaXPS software (version 2.3.26PR1.0). For the peak deconvolution, a Shirley-type background was used. For the XPS analysis of the powder, a small amount was spread on a Cu tape, while the spray-deposited films were directly placed on the sample holder using the Cu tape, and a calibration using C1s at 285.0 eV was applied.

2.7 Atomic Force Microscopy

The surface topography of the coated WO_3-C-PBM and WO_3-S-PBM drop-casted layers on Ni plate substrates were characterized using AFM with the TOSCA 400 (Anton Paar Germany GmbH). Multistage data quantification (MSDQ), recently developed by us, was applied to accurately extract quantitative and representative surface features [8].

2.8 Scanning Electron Microscopy

The morphology of the WO_3-C-PBM and WO_3-S-PBM coatings on Ni plates was characterized using a Phenom desktop SEM from Thermo Fisher Scientific. SEM images were acquired in the secondary electron mode with an acceleration voltage of 15 KeV. The bulk composition of all coatings was analyzed using an in-built EDX detector in the SEM.

2.9 Contact angle measurements

Contact angles were measured using OCA15PRO equipment (Data Physics Instruments GmbH). The measurements were conducted using 1 M KOH as the probe liquid which was dropped at a drop-eject-rate of 5 μL s-1 onto the surface of interest.

2.10 Hansen solubility parameters (HSP)

For determination of HSP, powders after planetary ball milling, WO_3-C-PBM and WO_3-S-PBM, were dispersed in probe liquids by ultrasonic homogenization (Branson SFX550). The probe liquids were selected according to the two-step procedure developed by Amin et al. [36]. In the first step, Ethanol (EtOH), Dimethylformamide (DMF), and Tetrahydrofuran (THF) were used to identify liquids that form good dispersions with the WO_3-C-PBM and WO_3-S-PBM powders. Based on the stability of the dispersion in the first step, additional probe liquids were screened in the second step, and the resulting probe liquid list was used to make the ranking for HSP determination according to Süß et al. [9].

Analytical centrifugation was used to sediment the dispersions using centrifugal acceleration. The dispersions were filled into polyamide and polycarbonate cells with 2 mm path length and inserted into a LUMisizer LS651 (LUM GmbH) analytical centrifuge and centrifuged at 2500 rpm for 20 h at 20 °C using 410 nm wavelength light. After the measurement, transmission fingerprints were generated by resolving the measurement time and position. Furthermore, transmittograms were plotted from the sedimentation data as well as described by Bapat et al.[2].

2.11. Ink formulation

Catalyst inks for anode preparation were generated in the following way: first 3 mg of the WO_3-C-PBM and WO_3-S-PBM powders were measured into a centrifuge tube followed by the addition of 1.5 mL water and 1.5 mL of an IPA:water mixture (volume ratio 1:1 r.t.p). The so-obtained suspension was homogenized by applying 6 min of probe sonication (Hielscher UP200Ht, Germany, ultrasonic homogenizer operating at 26 kHz, 40 % amplitude) [1] in two equal intervals of 3 min. Before commencing the last round of sonication, a small amount of Sustainion (20 wt%) was also added to the mixture. During the probe sonication, the ink was kept inside an ice bath to avoid evaporation.

2.12. Beaker cell electrochemical measurements

A three-electrode beaker cell coupled with VSP potentiostat VMP3 (BioLogic, France) was used for the electrochemical characterization. The working electrode was a Ni rod of area 0.07 cm2. Hg/HgO in 1 M KOH was used as the reference electrode and a spiral Pt wire was used as the counter electrode. All experiments were carried out in 100 ml of 1 M KOH (pellets, 85 % Sigma-Aldrich). The sample dispersion had a concentration of 3 mg/3 mL, and a total volume of 14.2 µL was drop casted onto the substrate in five successive steps of 2.64 µL each. Before drop casting, the Ni rods were cleaned with 1 µm, 0.3 µm and 0.05 µm alumina consecutively on a micro cloth. After each step, the Ni rod and was sonicated in ultrapure water for 5 minutes after each step.

The experiments were started by measuring the open circuit potential (OCP) for 60 seconds. The uncompensated resistance (Ru) was measured by the Potentiostatic electrochemical impedance spectroscopy (PEIS) performed over a frequency period of 100 kHz to 10 Hz with 10 rms AC voltage. The impedance was determined by considering the point where the phase angle reaches a minimum and is used for the iR correction with respect to reversible hydrogen electrode (RHE). 50 cyclic voltammograms were performed in a potential range of 0.400 to 1.600 V vs. RHE at a scan rate of 100 mV s-1 as a pre-conditioning step to minimize the impurities as well as to establish a steady stable state. The lLinear sweep voltammetry (LSV) was subsequently performed at a scan rate of 5 mVs-1 in a potential range of 1.300 V to 1.800 V vs. RHE.

The electrochemically active surface area (ECSA) was estimated from electrochemical impedance spectroscopy (EIS) measurements conducted at open-circuit potential (OCP). The impedance spectra were fitted using a two-element equivalent electrical circuit (EEC) consisting of Ru and a constant phase element (CPE) accounting for the charging and

discharging processes of the electrochemical double layer. The effective double-layer capacitance was derived from the CPE parameter (Q1) using the relationship described in the Results and Discussion section Chapter 3. Subsequently, the ECSA was calculated by dividing the effective capacitance with the specific capacitance (Cs) where Cs = 40 μF cm^{-2} [3].

3. References

1. Kräenbring, M.-A., F. Ozcan, and D. Segets, *Analyzing Emulsion Dynamics via Direct Visualization and Statistical Methodologies.* ACS omega, 2024. **9**(37): p. 39253-39258.
2. Bapat, S. and D. Segets, *Sedimentation dynamics of colloidal formulations through direct visualization: implications for fuel cell catalyst inks.* ACS Applied Nano Materials, 2020. **3**(8): p. 7384-7391.
3. McCrory, C.C., et al., *Benchmarking hydrogen evolving reaction and oxygen evolving reaction electrocatalysts for solar water splitting devices.* Journal of the American Chemical Society, 2015. **137**(13): p. 4347-4357.
4. Orazem, M.E. and B. Tribollet, *Electrochemical impedance spectroscopy.* New Jersey, 2008. **1**(906): p. 383-389.
5. Trasatti, S. and O. Petrii, *Real surface area measurements in electrochemistry.* Journal of electroanalytical chemistry, 1992. **327**(1-2): p. 353-376.
6. Yang, X., et al., *xPDFsuite: an end-to-end software solution for high throughput pair distribution function transformation, visualization and analysis.* arXiv preprint arXiv:1402.3163, 2014.
7. Farrow, C., et al., *PDFfit2 and PDFgui: computer programs for studying nanostructure in crystals.* Journal of Physics: Condensed Matter, 2007. **19**(33): p. 335219.
8. Jain, A., et al., *From Small-Area Observations to Insight: Surface-Feature-Extrapolation of Anodes for Alkaline Oxygen Evolution Reaction.* ChemCatChem, 2024. **16**(5): p. e202301461.
9. Süß, S., et al., *Determination of Hansen parameters for particles: A standardized routine based on analytical centrifugation.* Advanced Powder Technology, 2018. **29**(7): p. 1550-1561.